

# Can large strains be accommodated by small faults: “Brittle flow of rocks’ revised

Xiaoyu Zou<sup>1</sup> and Yuri Fialko<sup>2</sup>

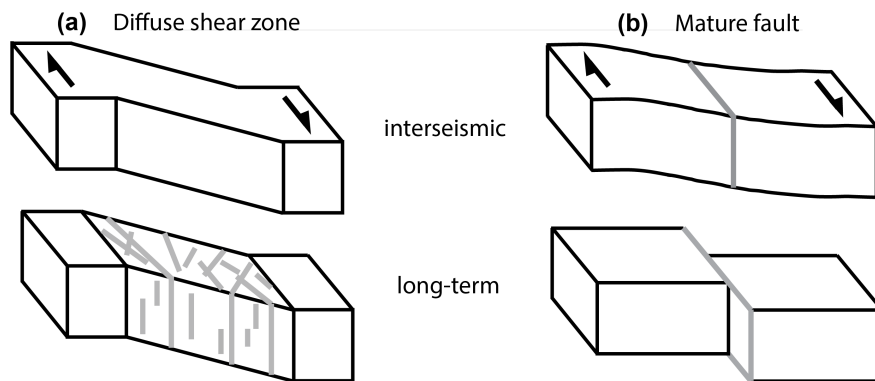
<sup>1</sup>Institute of Geophysics and Planetary Physics, Scripps Institute of Oceanography, UC San Diego

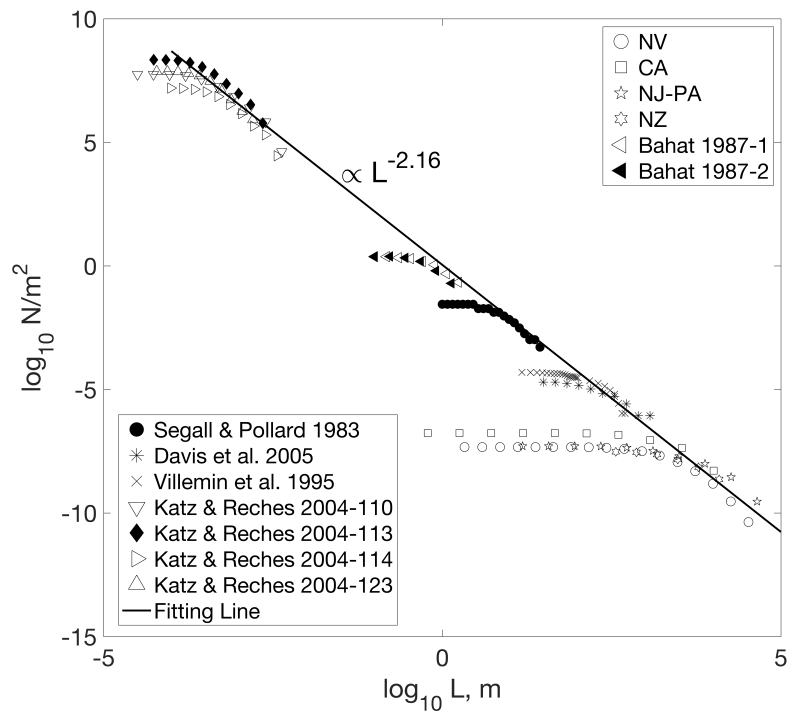
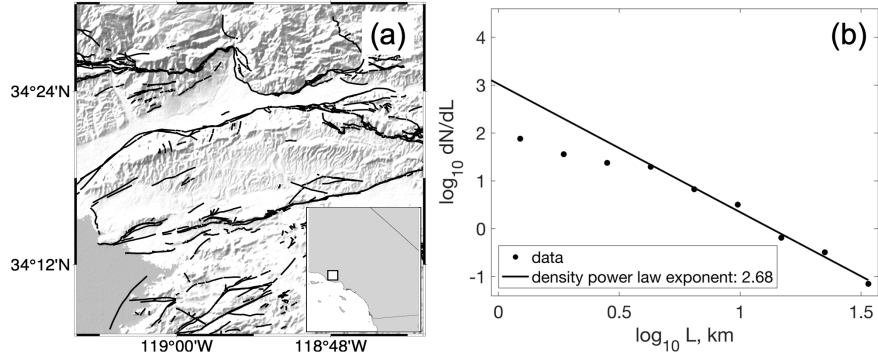
<sup>2</sup>UCSD

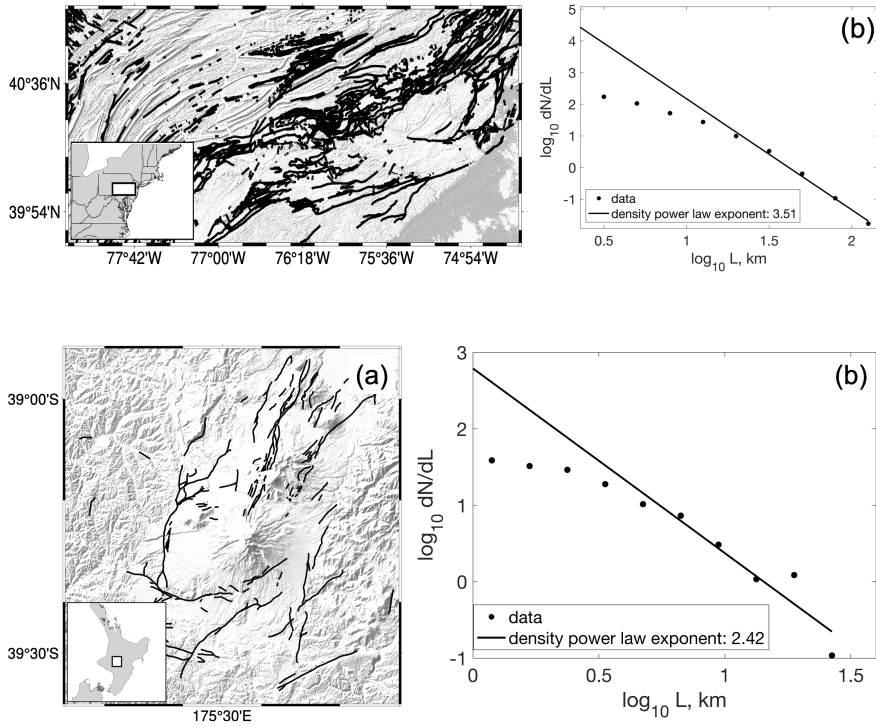
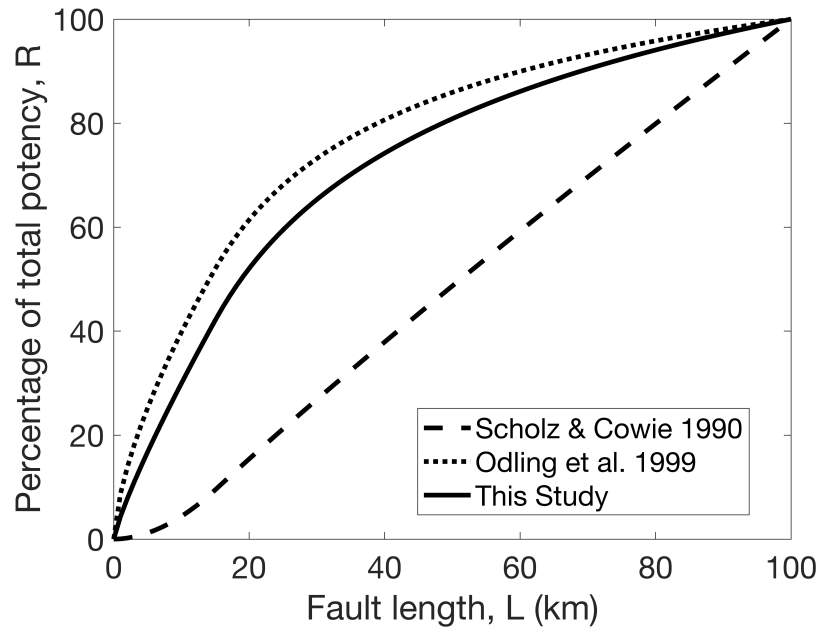
April 16, 2024

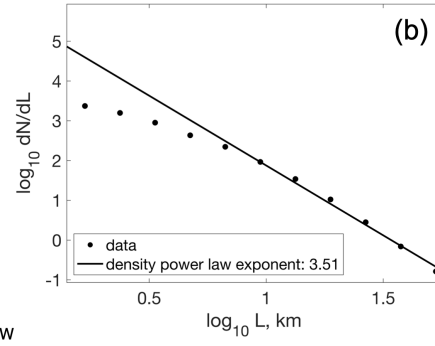
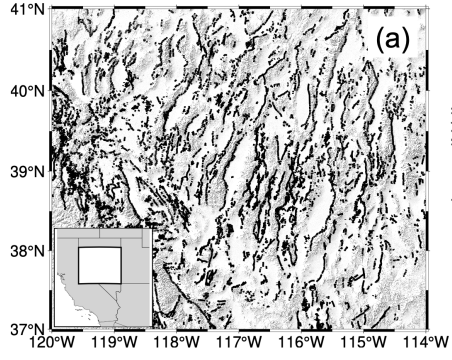
## Abstract

Brittle deformation in the upper crust is thought to occur primarily via faulting. The fault length-frequency distribution determines how much deformation is accommodated by numerous small faults vs a few large ones. To evaluate the amount of deformation due to small faults, we analyze the fault length distribution using high-quality fault maps spanning a wide range of spatial scales from a laboratory sample to an outcrop to a tectonic domain. We find that the cumulative fault length distribution is well approximated by a power law with a negative exponent close to 2. It follows that faulting is a self-similar process, and a substantial fraction of tectonic strain can be accommodated by faults that don’t cut through the entire brittle layer, consistent with inferences of “hidden strain’ from natural and laboratory observations. A continued accumulation of tectonic strain may eventually result in a transition from self-similar fault networks to localized mature faults.









1       **Can large strains be accommodated by small faults:**  
2               **“Brittle flow of rocks” revised**

3                               **Xiaoyu Zou<sup>1</sup>, Yuri Fialko<sup>1</sup>**

4       <sup>1</sup>Institute of Geophysics and Planetary Physics, Scripps Institution of Oceanography, University of  
5                               California San Diego, La Jolla, CA 92093, USA.

6       **Key Points:**

- 7       • We analyze the fault length-frequency distribution in developing (structurally im-  
8               mature) fault systems.
- 9       • The cumulative frequency distribution follows a power law over a range of fault  
10              lengths spanning 8 orders of magnitude, with a negative power-law exponent of  
11               $\sim 2$ , implying scale independence.
- 12       • Small faults within the brittle upper crust can accommodate a substantial ( $> 30\%$ )  
13              fraction of tectonic strain.

## Abstract

Brittle deformation in the upper crust is thought to occur primarily via faulting. The fault length-frequency distribution determines how much deformation is accommodated by numerous small faults vs a few large ones. To evaluate the amount of deformation due to small faults, we analyze the fault length distribution using high-quality fault maps spanning a wide range of spatial scales from a laboratory sample to an outcrop to a tectonic domain. We find that the cumulative fault length distribution is well approximated by a power law with a negative exponent close to 2. It follows that faulting is a self-similar process, and a substantial fraction of tectonic strain can be accommodated by faults that don't cut through the entire brittle layer, consistent with inferences of "hidden strain" from natural and laboratory observations. A continued accumulation of tectonic strain may eventually result in a transition from self-similar fault networks to localized mature faults.

## Plain language summary

The Earth's crust is pervasively damaged, and contains faults of various sizes and orientations. We use mapped fault traces from multiple data sets spanning a wide range of scales to investigate how much deformation is accommodated by small vs large faults. The fault length distribution is often assumed to be fractal, i.e., following a power law. The power-law exponent  $\alpha$  quantifies the relative contributions of many small faults relative to a few large ones. For  $\alpha \leq 1$ , the contribution of small faults is negligible, while for  $\alpha \geq 2$ , strains accommodated by small faults become significant. We find that the cumulative fault length distribution approximately follows a power law with an exponent close to 2. This implies that small faults in developing shear zones can accommodate substantial tectonic strain.

## Introduction

Tectonic deformation in the brittle upper crust is mainly accommodated by faulting (e.g., S. Cox & Scholz, 1988). Faults are ubiquitous in both intraplate settings and at plate boundaries (e.g., Ojo et al., 2022; R. T. Cox et al., 2001; Rui & Stamps, 2019; Bürgmann & Pollard, 1994). As faults continue to slip, they increase their length via crack tip propagation, linkage, and coalescence (e.g., Mansfield & Cartwright, 2001; S. Cox & Scholz, 1988; Dawers & Anders, 1995; Fossen, 2020; Rotevatn et al., 2019). As a result,

45 the upper crust contains faults of various sizes, from millimeter-long microfractures to  
 46 mature faults extending hundreds of kilometers. The fault length distribution controls  
 47 the relative contributions of small vs large faults to a total strain budget and is of in-  
 48 terest to many disciplines including tectonics, engineering geology, hydrogeology, petroleum  
 49 industry, and seismic hazards assessment (e.g., C. H. Scholz & Cowie, 1990; Louderback,  
 50 1950; Bense et al., 2013; Bonnet et al., 2001).

51 Previous studies suggested a variety of functional forms describing the fault size  
 52 distribution. It is generally believed that in a low-strain environment (e.g., developing  
 53 shear zones), fault populations are fractal and thus follow a power-law distribution (e.g.,  
 54 Childs et al., 1990; Turcotte, 1986; Bour & Davy, 1999; Bonnet et al., 2001; Ben-Zion  
 55 & Sammis, 2003). Nicol et al. (1996) noted that the fault length distribution may de-  
 56 viate from a power-law if a wide range of fault lengths is considered, and that the power-  
 57 law exponent may vary at the low end of the fault length distribution owing to spatial  
 58 clustering. In contrast, Odling et al. (1999) argued that the fault length distribution may  
 59 appear as log-normal in individual data sets with a given detection threshold, but is a  
 60 power-law for “composite” data sets that combine a number of individual data sets span-  
 61 ning a wide range of spatial scales. Gupta and Scholz (2000) suggested a transition from  
 62 a power-law to an exponential distribution when tectonic strain exceeds a critical thresh-  
 63 old of the order of 0.1.

64 In case of a power-law distribution, the number of faults  $N$  that have lengths greater  
 65 than or equal to  $L$  is given by

$$N(L) = CL^{-\alpha} \quad (1)$$

66 where  $C$  is an empirical constant, and  $\alpha > 0$  is an absolute value of the power-law ex-  
 67 ponent, also known as the Pareto index (e.g., Clark et al., 1999). The derivative of the  
 68 cumulative fault length distribution (1) with respect to  $L$  is the probability density,

$$\frac{dN}{dL} = C(1 - \beta)L^{-\beta}, \quad (2)$$

69 which is also a power law, with  $\beta = \alpha + 1$ . The probability density (2) is sometimes  
 70 referred to as the non-cumulative frequency distribution. A number of studies used field  
 71 observations to test the assumption of a fractal distribution, and estimate parameters  
 72  $C$  and  $\alpha$  (or  $\beta$ ). Reported values of the best-fit power-law exponent  $\alpha$  vary from 0.7 for  
 73 faults in Chimney Rock, Utah (Krantz, 1988; Cladouhos & Marrett, 1996) to 1.1 for Neo-  
 74 gene faults in the Boso and Iura Peninsula, Japan (C. H. Scholz & Cowie, 1990) to 2.3

75 for faults and fractures in sandstone in Tayma, Saudi Arabia (Odling et al., 1999). Most  
76 of the previous studies used data sets consisting of  $10^2$ – $10^3$  fault traces with fault lengths  
77 spanning 1-2 decades.

78 The magnitude of the power-law exponent determines how deformation is parti-  
79 tioned between small and large faults. Kautz and Sclater (1988) argued, based on lab-  
80 oratory experiments and observations of natural faults, that small-scale faulting is re-  
81 sponsible for a substantial internal deformation within crustal blocks bounded by ma-  
82 jor faults. In contrast, C. H. Scholz and Cowie (1990) estimated the power-law exponent  
83  $\alpha \approx 1$  using fault trace data from Japan and argued that small faults are negligible in  
84 the total strain budget. Recently, Fialko and Jin (2021) suggested that high-angle con-  
85 jugate faults (“cross-faults”) in the Eastern California Shear Zone can result from a long-  
86 term relative rotation assisted by a distributed faulting. No such rotation would be pos-  
87 sible if small faults are too scarce to accommodate a substantial fraction of tectonic strain.

88 To quantify the amount of deformation that can be attributed to small-scale fault-  
89 ing, we analyze the fault length distribution across a wide range of spatial scales using  
90 several high-quality data sets. In particular, we use detailed fault maps from different  
91 geological settings, including the Basin and Range Province (Nevada), Central Pennsyl-  
92 vania/Northern New Jersey, Ventura County (California), and Northern New Zealand.  
93 We complement these crustal-scale data sets with outcrop-scale observations from East-  
94 ern Israel (Bahat, 1987), Sierra Nevada (Segall & Pollard, 1983), Southern New Zealand  
95 (Davis et al., 2005), and Eastern France (Villemin et al., 1995). We also use laboratory  
96 observations of microfractures in rock samples loaded to failure at confining pressures  
97 of several tens of megapascals (Katz & Reches, 2004). We examine the compiled multi-  
98 scale data to test the assumption of a power-law distribution, obtain the best-fit power-  
99 law exponent, and use the latter to estimate the amount of strain accommodated by faults  
100 in the upper crust, as a function of fault size.

## 101 **1 Data and Methods**

102 We are interested in the fault length-frequency distribution in regions of distributed  
103 deformation such as the Eastern California Shear Zone (Dokka & Travis, 1990; Tymo-  
104 fyeyeva & Fialko, 2015; Fialko & Jin, 2021). Unfortunately, developing (i.e., structurally  
105 immature) strike-slip faults are often difficult to recognize due to their limited geomor-

106 phologic expression, especially at the low end of fault sizes. Dip-slip fault systems are  
 107 better suited for this purpose. One of the most extensive and detailed fault trace data  
 108 sets from an actively deforming extensional region is that from the Basin and Range (B&R)  
 109 province in the Western US (Figure 1a). This region hosts a number of active Quater-  
 110 nary faults (e.g., Eaton, 1982; U.S. Geological Survey and Nevada Bureau of Mines and  
 111 Geology, 2023). We examine fault traces from an area extending 6 degrees in longitude  
 112 and 4 degrees in latitude (Figure 1a). The respective data set consists of 26512 fault traces,  
 113 with the fault segment lengths varying from 2.1 m to 42.6 km.

114 A close inspection of the B&R fault trace data reveals that many fault traces that  
 115 appear continuous on a regional scale (Figure 1a) are in fact highly segmented (Supple-  
 116 mentary Figure S1a). While some of the apparently continuous fault traces may be seg-  
 117 mented because they have different attributes such as dip and strike, others “may have  
 118 the same attributes but are still separated at the segment level” (R. Schmitt, USGS, per-  
 119 sonal communication). To mitigate potential biases due to artificial segmentation, we  
 120 developed an algorithm for concatenating individual segments that likely belong to the  
 121 same fault. The algorithm attributes different segments to the same fault if the follow-  
 122 ing criteria are satisfied: (1) tips of the adjacent fault segments are within a prescribed  
 123 distance  $D$  from each other; (2) the adjacent fault segments are sufficiently well aligned,  
 124 such that the difference in strike angles  $\theta_1$  and  $\theta_2$  between the segment tips (see Figure  
 125 S2a) is less than a prescribed threshold  $\delta$ ; also, we require that the difference between  
 126 the average of strike angles at the segment tips,  $(\theta_1 + \theta_2)/2$  and the strike angle of a line  
 127 connecting the segment tips is less than a prescribed threshold  $\delta$  (Figure S2c); (3) over-  
 128 lapping segments that satisfy conditions (1) and (2) are considered part of the same fault  
 129 if  $D < L/3$ , where  $L$  is the length of a smaller segment. The latter condition is meant  
 130 to avoid absorption of small faults that are sub-parallel to (rather than aligned with) the  
 131 large ones. The respective criteria are illustrated in Figure S2.

132 A reasonable upper limit on  $D$  is some fraction of the thickness of the brittle layer  
 133  $T$ , such that the apparently discontinuous (e.g., poorly exposed) surface traces might pos-  
 134 sibly belong to the same fault at depth. For the Basin and Range province,  $T \approx 15$  km  
 135 (e.g., Pancha et al., 2006). We assume  $D < (T/3 = 5$  km). We find that the best-fit  
 136 power-law exponent is relatively insensitive to the assumed value of  $D$ , for  $\delta$  between 0  
 137 and 30 degrees (Figures S3 and S4). Larger values of  $D$  and  $\delta$  encourage segment link-  
 138 ing, resulting in a smaller number of small faults, and consequently smaller absolute val-

139 ues of the best-fit power-law exponents. In the analysis presented below, we use  $D =$   
 140 5 km, and  $\delta = 30^\circ$  to provide a lower bound on  $\alpha$ . A comparison of fault trace data  
 141 before and after "de-segmentation" is shown in Figure S1.

142 Because the cumulative fault length distribution is known to be sensitive to finite  
 143 size effects, which can potentially bias determination of the exponent (e.g., Bonnet et  
 144 al., 2001), we use the density distribution (equation 2) to estimate the power-law expo-  
 145 nent  $\beta$ , unless indicated otherwise. The respective values of  $\alpha$  are trivially given by  $\alpha =$   
 146  $\beta - 1$ .

147 Figure 1b shows the probability density of fault length distribution for the "con-  
 148 catenated" Basin and Range data set (a subset is shown in Figure S1b). To minimize  
 149 the censoring bias (e.g., Torabi & Berg, 2011), we refine the data set by excluding faults  
 150 that intersect the region boundaries. On a log-log plot, the density distribution exhibits  
 151 a quasi-linear trend for  $L > 5$  km, and flattens out for smaller  $L$ . The roll-off at  $L <$   
 152 5 km likely results from incomplete sampling (truncation bias, Torabi & Berg, 2011; Bon-  
 153 net et al., 2001), analogous to saturation of the Gutenberg-Richter distribution below  
 154 the magnitude of completeness (e.g., Woessner & Wiemer, 2005). The truncation bias  
 155 may be due to a finite detection threshold and/or 2-D sampling of a 3-D fault popula-  
 156 tion (e.g., Heifer & Bevan, 1990). We use the Kolmogorov-Smirnov (KS) test (Clauset  
 157 et al., 2009) to identify the range of fault lengths  $[L_{min}, L_{max}]$  that can be used for power-  
 158 law fitting (see Supplementary Text S1 for details). We estimate the density power-law  
 159 exponent  $\beta$  by the least-squares linear regression over the interval  $[L_{min}, L_{max}]$ . The un-  
 160 certainty on the best-fit slope is obtained by performing a regression for different bin sizes,  
 161 and computing a standard deviation of the resulting slope estimates. For the data shown  
 162 in Figure 1, we obtain  $\beta = 3.51 \pm 0.12$ , or  $\alpha \approx 2.5$ . This can be compared to the value  
 163 of  $\alpha = 1.84$  estimated by Cladouhos and Marrett (1996), who used an older (presum-  
 164 ably, less complete) fault map of the Basin and Range province, and fitted a linear trend  
 165 to the cumulative fault length distribution over the fault length interval between  $\sim 15$ -  
 166 70 km.

167 We extended the same analysis to several other locations for which high-resolution  
 168 maps of dip-slip faults are openly available, in particular, Central Pennsylvania and North-  
 169 ern New Jersey, Ventura County (California), and Northern New Zealand. Figure 2a shows  
 170 fault traces from an area in Central Pennsylvania and Northern New Jersey (PA Depart-

171 ment of Conservation & Natural Resources, 2023; NJ Dept. of Environmental Protec-  
 172 tion Bureau of GIS, 2023). The mapped traces represent inactive thrust and strike-slip  
 173 faults formed 400 to 250 million years ago (Hatcher, 1987). For consistency, we apply  
 174 the same algorithm for concatenating the aligned segments as described above. The re-  
 175 sulting data set consists of 2273 faults having length between 15 m and 108 km. The prob-  
 176 ability density fault length distribution (Figure 2b) is characterized by an apparent trun-  
 177 cation for faults smaller than 20 km, and a slope of the quasi-linear trend of  $-3.51$ , re-  
 178 markably similar to results obtained for the Basin and Range province (Figure 1b).

179 The Ventura County, CA (Figure 3) and Northern New Zealand (Figure 4) fault  
 180 maps cover much smaller areas. After the segment concatenation procedure, each data  
 181 set contains several hundreds of fault traces. This is 1-2 orders of magnitude smaller than  
 182 the number of fault traces in the B&R and Pennsylvania/New Jersey data sets (Figures 1  
 183 and 2), but comparable to a typical size of data sets examined in a number of previous  
 184 studies. While these smaller data sets are too characterized by decaying trends toward  
 185 the high end of the sampled range of fault lengths, the data exhibit a significant scat-  
 186 ter (e.g., Figure 4b), making power-law fits more problematic. Our analysis of the re-  
 187 spective data sets yields smaller values of  $\beta$  that are subject to higher uncertainties ( $2.68 \pm$   
 188  $0.14$  for Ventura County and  $2.42 \pm 0.40$  for Northern New Zealand, see Figures 3b and 4b).

189 To evaluate the fault length distribution at smaller scales, we use published data  
 190 on fracture density measured in outcrops ( $L \sim 1-100$  m) and laboratory samples ( $L \sim 1-$   
 191  $100$  mm). The outcrop-scale observations include joints in Eocene chalks in the Syrian  
 192 Arc folding belt, Israel (Bahat, 1987); joints in igneous rocks near Florance Lake, Sierra  
 193 Nevada, California (Segall & Pollard, 1983); thrust faults in the Ostler Fault Zone, Ben-  
 194 more outcrop, Southern New Zealand (Davis et al., 2005); and predominantly dip-slip  
 195 faults in La Houve Coal Field, an old sedimentary basin in Eastern France that expe-  
 196 rienced both compressional and extensional tectonics (Villemin et al., 1995). The lab-  
 197 oratory data are from specimens of Mount Scott granite of Oklahoma loaded to peak yield  
 198 stress in a triaxial apparatus under confining pressure of 41 MPa (Katz & Reches, 2004).  
 199 The micro-structural mapping of the sample damage was performed on scanned images  
 200 of thin sections. Each sample had on the order of  $10^3$  resolved micro-fractures with lengths  
 201 between 0.01-10 mm (Katz & Reches, 2004).

202 A compilation of the respective data sets is presented in Figure 5, along with the  
 203 fault trace data from Figures 1-4. To enable a direct comparison of different data sets,  
 204 we normalize the cumulative fault length counts by the areas from which the fault trace  
 205 data were collected. The combined cumulative frequency distribution spans 8 decades  
 206 of fault length, and 18 decades of fault density (cumulative fault counts per unit area).  
 207 All of the individual data sets shown in Figure 5 appear to have a log-normal distribu-  
 208 tion, with a quasi-linear trend at the high end, and a roll-off at the low end of the re-  
 209 spective fault lengths. However, the combined data set admits a common envelope, with  
 210 a slope that closely matches those of most of individual data sets. The least squares fit  
 211 of the common envelope (see solid black line in Figure 5) yields a power-law exponent  
 212 of  $\alpha \approx 2.16$ .

## 213 **2 Strain due to faults obeying a power law distribution**

214 An overall agreement of the estimated power-law exponents of individual data sets  
 215 between each other, on the one hand, and the common envelope, on the other hand (Fig-  
 216 ure 5), lends support to a suggestion that the roll off in individual data sets is a result  
 217 of truncation (e.g., due to a detection threshold, Bonnet et al., 2001; Torabi & Berg, 2011),  
 218 and that the fault length statistics is adequately described by a power law across a wide  
 219 range of spatial scales. If so, one can evaluate the amount of tectonic strain absorbed  
 220 by faults of different sizes (e.g., C. H. Scholz & Cowie, 1990; J. Walsh et al., 1991).

221 For a population of  $n$  faults within the brittle crust having a volume  $TA$ , where  
 222  $T$  is the thickness of the brittle layer, and  $A$  is the map area, the average strain accom-  
 223 modated by faulting is given by (Kostrov, 1974):

$$\varepsilon_{ij} = \frac{1}{2TA} \sum_{k=1}^n {}^k P_{ij}. \quad (3)$$

224 In equation (3),  ${}^k P_{ij}$  is the seismic potency tensor (e.g., Ben-Zion, 2001) of the  $k$ -th fault  
 225 in a population. The average fault slip  $S$  is expected to scale with fault length  $L$ ,

$$S \propto L^m. \quad (4)$$

226 Theoretical arguments and field observations suggest that  $m$  should be close to 1 (e.g.,  
 227 Cowie & Scholz, 1992; Fialko, 2015), although higher values of  $m$  were suggested as well  
 228 (e.g., J. J. Walsh & Watterson, 1988; Marrett & Allmendinger, 1991). Assuming  $m =$

229 1,

$$S = \epsilon L, \quad (5)$$

230 where  $\epsilon$  is the critical shear strain drop corresponding to fault propagation. The scalar  
 231 potency is  $P = \gamma SL^2$  for faults smaller than  $T$ , and  $P = \gamma SLT$  otherwise, where  $\gamma$  is  
 232 a geometric factor of the order of unity that accounts for the fault shape and fault dip  
 233 (for faults that cut through the entire brittle layer, e.g., Vavra et al., 2023). For simplic-  
 234 ity, hereafter we assume  $\gamma = 1$ . The number of faults within an interval of fault lengths  
 235  $\Delta L$  is  $(dN(L)/dL)\Delta L$ . The cumulative potency can be calculated by integrating poten-  
 236 cies of all faults for a given range of fault lengths. For faults smaller than  $T$ , the cumu-  
 237 lative potency is (C. H. Scholz & Cowie, 1990):

$$p_1(L_{min}, L_{max}) = \sum_k {}^k P = -\epsilon \int_{L_{min}}^{L_{max}} \frac{dN(L)}{dL} L^3 dL = C\epsilon \frac{\alpha}{3-\alpha} L^{3-\alpha} \Big|_{L_{min}}^{L_{max}}, \quad (6)$$

238 where  $L_{min}$  and  $L_{max}$  are the minimum and maximum fault sizes, respectively. For faults  
 239 that cut through the entire brittle layer ( $L > T$ ),

$$p_2(L_{min}, L_{max}) = \sum_k {}^k P = -\epsilon T \int_{L_{min}}^{L_{max}} \frac{dN(L)}{dL} L^2 dL = C\epsilon T \frac{\alpha}{2-\alpha} L^{2-\alpha} \Big|_{L_{min}}^{L_{max}}. \quad (7)$$

240 We evaluate the relative contribution of faults smaller than a given size  $L$  to the total  
 241 strain by allowing  $L_{min} \rightarrow 0$ , and computing a ratio

$$R = 100\% \times \begin{cases} \frac{p_1(0,L)}{p_1(0,T)+p_2(T,L_{max})}, & \text{for } L < T \\ \frac{p_1(0,T)+p_2(T,L)}{p_1(0,T)+p_2(T,L_{max})}, & \text{for } L > T. \end{cases} \quad (8)$$

242 Note that  $R$  does not depend on factors  $C$  and  $\epsilon$ . Figure 6 shows the percentage of strain  
 243 accommodated by faults having length less than  $L$ , for a range of  $L$ , assuming  $\alpha = 2.16$ ,  
 244  $L_{max} = 100$  km (Figure 5), and  $T = 15$  km, typical of the seismogenic depth in many  
 245 tectonically active areas (e.g., Pancha et al., 2006; E. O. Lindsey & Fialko, 2016; Jin et  
 246 al., 2023; Jia et al., 2023). For a comparison, we also show analogous calculations for pre-  
 247 viously reported values of  $\alpha = 1.1$  (dashed line, C. H. Scholz & Cowie, 1990) and  $\alpha =$   
 248  $2.34$  (dotted line, Odling et al., 1999).

### 249 3 Discussion

250 For fault systems characterized by a power-law size distribution (1), the power-law  
 251 exponent  $\alpha$  controls how much of tectonic deformation is accommodated by numerous  
 252 small faults versus a few large ones. C. H. Scholz and Cowie (1990) estimated the value

253 of  $\alpha = 1.1$  for a set of intraplate faults in Japan, and concluded that small faults are  
254 negligible in the overall strain budget. This is because integrals (6) and (7) are strongly  
255 convergent for  $\alpha \approx 1$ , so that the cumulative potency is dominated by the largest faults.  
256 Our results, based on a much larger data set, indicate  $\alpha \geq 2$  (Figure 5). Most of the  
257 previously published estimates of  $\alpha$  fall in the range between 1 and 2 (e.g., Bonnet et  
258 al., 2001). Possible reasons for different values of  $\alpha$  reported in the literature include:  
259 (i) use of fault trace data of limited coverage and/or resolution; (ii) uncertainties involved  
260 in defining fault connectivity; (iii) a narrow range of fault lengths used in the analysis;  
261 (iv) departures from self-similarity due to the presence of intrinsic length scales; (v) dif-  
262 ferent stages of maturity of different fault systems. For example, the data set used by  
263 C. H. Scholz and Cowie (1990) spans only one order of magnitude of fault lengths, from  
264  $\sim 10$  to  $\sim 100$  km, likely insufficient for a robust validation of a power-law distribution  
265 (Stumpf & Porter, 2012). C. Scholz et al. (1993) analyzed a data set from the Volcanic  
266 Tableland (California) with fault lengths spanning 2 orders of magnitude, from a few tens  
267 of meters to a few kilometers, and obtained a higher value of  $\alpha \approx 1.3$ . The latter under-  
268 predicts the slope at the upper tail of the fault length distribution of C. Scholz et al. (1993,  
269 their figure 4), which the authors attributed to data censoring.

270 Our analysis of several high-resolution data sets (Figures 1-5) suggests values of  
271  $\alpha$  close to 2, higher than those reported by C. H. Scholz and Cowie (1990) and C. Scholz  
272 et al. (1993), but consistent with results from other multi-resolution studies. In partic-  
273 ular, Heifer and Bevan (1990) combined fault trace data with measurements of crack den-  
274 sity in boreholes to infer  $\alpha \approx 2$ . Odling et al. (1999) performed a multi-scale analysis  
275 of the length distribution of faults in sandstones in Saudi Arabia, and found the best-  
276 fit power-law exponent of 2.34 for a range of fault lengths spanning 4 orders of magni-  
277 tude. C. Scholz et al. (1993) cautioned against combining observations that include dif-  
278 ferent fracture modes (e.g., faults and joints, Heifer & Bevan, 1990). However, it can  
279 be argued that the crack length distributions should not strongly depend on the frac-  
280 ture mode as mathematical expressions for stress fields due to shear and tensile cracks  
281 are essentially identical (e.g., Fialko, 2015), so that stress interactions within the crack  
282 network are expected to be similar (e.g., for shear and tensile cracks). An overall agree-  
283 ment between the estimated power-law exponents for different types of fractures, as well  
284 as for data sets from different locations (Figure 5) lends support to a hypothesis that

285 faulting is governed by a "universal" power law with  $\alpha \approx 2$  (King, 1983; Proekt et al.,  
 286 2012; Roman & Bertolotti, 2022), at least at the initial stages of failure.

287 We point out that the data set used by C. H. Scholz and Cowie (1990) is dominated  
 288 by "long" ( $L > T$ ) faults that accumulated a substantial amount of slip, and thus might  
 289 be more representative of a structurally mature fault system. Experimental studies in-  
 290 deed reveal higher values of  $\alpha$  at the initial stages of faulting when deformation is broadly  
 291 distributed, and a decrease to  $\alpha \approx 1$  with an increasing system maturity (e.g., Sornette  
 292 et al., 1993; Hatton et al., 1993; Cladouhos & Marrett, 1996). It follows that small faults  
 293 can potentially accommodate a substantial fraction of tectonic strain at the initial stages  
 294 of faulting (e.g., in developing shear zones). Over time, as faults grow and connect, de-  
 295 formation may localize to major faults that eventually take up most of the deformation.

296 These arguments suggest an important distinction between deformation styles due  
 297 to immature shear zones such as the Eastern California Shear Zone (Dokka & Travis,  
 298 1990; Floyd et al., 2020), and mature well-slipped plate boundary faults such as the San  
 299 Andreas Fault (Lisowski et al., 1991; Fialko, 2006). In the latter case, interseismic strain  
 300 accumulation is equal in magnitude, but opposite in sign to strain released in large earth-  
 301 quakes, so the patterns of interseismic and long-term (geologic) displacements across a  
 302 mature fault are very different (Figure 7). A complete or nearly complete recovery of in-  
 303 terseismic strain (i.e., elastic rebound) is evidenced by good agreement between "geo-  
 304 logic" and "geodetic" slip rates on major plate boundary faults (e.g., Schmalzle et al.,  
 305 2006; Tatar et al., 2012; E. Lindsey & Fialko, 2013). In contrast, immature fault systems  
 306 with  $\alpha \geq 2$  give rise to a distributed inelastic deformation with the long-term displace-  
 307 ment profile that may closely mimic the observed interseismic velocities (Fialko & Jin,  
 308 2021). The diffuse deformation pattern illustrated in Figure 7a can be thought of as re-  
 309 sulting from the "seismic flow of rocks", as originally envisioned by Riznichenko (1965)  
 310 and Kostrov (1974), although a more appropriate term would be the "brittle flow of rocks",  
 311 since some of the deformation may occur aseismically, e.g. via creep (Tymofeyeva et  
 312 al., 2019; Kaneko et al., 2013) or the bulk yielding (Donath & Parker, 1964; Hamiel et  
 313 al., 2006).

314 The relative contribution of small faults to the strain budget is expected to be larger  
 315 for smaller values of  $L_{max}$ , and/or larger values of  $\alpha$ . We note that the estimated val-  
 316 ues of  $\alpha$  may in fact be lower bounds due to two-dimensional (2-D) sampling of three-

317 dimensional (3-D) fault populations. For example, for uniformly distributed and randomly  
318 oriented faults, the true (i.e., 3-D) exponent is predicted to be larger than the exponent  
319 inferred from the 2-D sampling by as much as 1 unit (e.g., Bonnet et al., 2001; Marrett  
320 & Allmendinger, 1991). This only applies to small ( $L < D$ ) faults, as for large faults  
321 the distribution is essentially 2-D. For  $\alpha$  approaching 3, small faults would actually dom-  
322 inate the strain budget, and the contribution of large faults would be negligible. Note  
323 that for the cumulative potency and strain to remain finite,  $\alpha$  cannot exceed 3 (eq. 6).

324 Taking at face value the estimated power law-exponent  $\alpha \approx 2$  (Figure 5), we find  
325 that small ( $L < T$ ) faults may take up more than one third of the total strain, which  
326 is almost an order of magnitude greater than predicted for  $\alpha \approx 1$  (Figure 6). A power  
327 law-exponent  $\alpha \geq 2$  may provide an explanation for the “missing strain” in palinspas-  
328 tic restorations of faults in sedimentary basins, as well as in laboratory models of tec-  
329 tonic extension using analog materials (e.g., Kautz & Sclater, 1988; Marrett & Allmendinger,  
330 1992; J. Walsh et al., 1991). The bulk inelastic deformation accommodated by small faults  
331 can result in rotation of faults away from the optimal orientation, and increases in di-  
332 hedral angles between conjugate faults, as often observed in active shear zones (e.g., Ron  
333 et al., 2001; Fialko, 2021; Zou et al., 2023). It might also account for the reported dif-  
334 ferences between geologic and geodetic slip rates in regions of diffuse deformation. In par-  
335 ticular, models of deformation across the plate boundary in California suggest that up  
336 to 30% of deformation is accommodated off of the known faults (Field et al., 2014). Sim-  
337 ilar conclusions are drawn from numerical models of continental extension (Pan et al.,  
338 2023). Given no resolvable difference between the geologic and geodetic slip rates of ma-  
339 ture high-slip-rate faults such as the San Andreas and San Jacinto faults (Segall, 2002;  
340 E. O. Lindsey et al., 2014; Tymofyeyeva & Fialko, 2018; Schmalzle et al., 2006), most  
341 of the “missing slip” is apparently associated with regions of diffuse deformation char-  
342 acterized by low strain rates such as the Eastern California Shear Zone (Herbert et al.,  
343 2014). The same may apply to other areas of broadly distributed continental deforma-  
344 tion such as the India-Eurasia collision zone (e.g., Garthwaite et al., 2013; Wang & Shen,  
345 2020). Finally, we note that the non-negligible contributions of small faults to finite strain  
346 suggested by our analysis contrasts with the seismic moment release which is strongly  
347 dominated by largest events (e.g., Bell et al., 2013). This is likely due to the fact that  
348 only a fraction of faults that exist within the seismogenic zone are seismically active at  
349 any given time. One mechanism for eventual de-activation of pre-existing or newly formed

350 faults is rotation of fault planes away from the principal compression axis with increas-  
 351 ing finite strain (e.g., Ron et al., 2001; Fialko & Jin, 2021; Zou et al., 2023).

## 352 4 Conclusions

353 We analyzed the fault length frequency distribution using high-resolution fault trace  
 354 data from diverse settings including Basin and Range Province, Central Pennsylvania/Northern  
 355 New Jersey, Ventura County, California, and Northern New Zealand. To extend our anal-  
 356 ysis to smaller scales, we included published outcrop data from Sierra Nevada, Eastern  
 357 Israel, Southern New Zealand, and Eastern France, and laboratory data from experiments  
 358 on the initially intact granite samples. Our results indicate that while each individual  
 359 data set yields an apparent log-normal distribution of fault lengths, a composite multi-  
 360 scale data set reveals a fault length-distribution that follows a power law over 8 decades  
 361 of fault lengths, with a cumulative power-law exponent  $\alpha \approx 2$ . The obtained best-fit  
 362 value may be an under-estimate of the true value of the power-law exponent given an  
 363 observation bias (2-D sampling of 3-D faults). We used the best-fit value of the power-  
 364 law exponent to estimate a fraction of strain accommodated by faults as a function of  
 365 fault size. We find that small faults ( $L < 15$  km) can accommodate a substantial (up  
 366 to 40%) fraction of tectonic strain, at least at the initial stages of faulting. A continued  
 367 deformation may give rise to a transition from self-similar fault networks to highly lo-  
 368 calized mature faults.

## 369 Acknowledgments

370 We thank reviewers... This study was supported by NSF (EAR-1841273) and NASA (80NSSC22K0506).  
 371 Figures were produced using Generic Mapping Tools (GMT) (Wessel et al., 2013) and  
 372 Matlab. The authors declare no competing interests.

## 373 Data Availability Statement

374 The fault trace data used in this paper are available at [10.5281/zenodo.10938802](https://doi.org/10.5281/zenodo.10938802).

## 375 References

- 376 Bahat, D. (1987). Jointing and fracture interactions in Middle Eocene chalks near  
 377 Beer Sheva, Israel. *Tectonophysics*, *136*(3), 299-321.
- 378 Bell, A. F., Naylor, M., & Main, I. G. (2013). Convergence of the frequency-size dis-

- 379           tribution of global earthquakes. *Geophys. Res. Lett.*, *40*(11), 2585–2589.
- 380 Bense, V., Gleeson, T., Loveless, S., Bour, O., & Scibek, J. (2013). Fault zone hydrogeology. *Earth-science reviews*, *127*, 171-192.
- 381
- 382 Ben-Zion, Y. (2001). On quantification of the earthquake source. *Seismol. Res. Lett.*,  
383           *72*(2), 151–152.
- 384 Ben-Zion, Y., & Sammis, C. G. (2003). Characterization of fault zones. *Pure Appl.*  
385           *Geophys.*, *160*(3), 677–715.
- 386 Bonnet, E., Bour, O., Odling, N. E., Davy, P., Main, I., Cowie, P., & Berkowitz, B.  
387           (2001). Scaling of fracture systems in geological media. *Reviews of Geophysics*,  
388           *39*(3), 347-383.
- 389 Bour, O., & Davy, P. (1999). Clustering and size distributions of fault patterns:  
390           Theory and measurements. *Geophys. Res. Lett.*, *26*(13), 2001-2004.
- 391 Bürgmann, R., & Pollard, D. D. (1994). Strain accommodation about strike-slip  
392           fault discontinuities in granitic rock under brittle-to-ductile conditions. *J.*  
393           *Struct. Geol.*, *16*(12), 1655-1674.
- 394 Childs, C., Walsh, J. J., & Watterson, J. (1990). A method for estimation of the  
395           density of fault displacements below the limits of seismic resolution in reservoir  
396           formations. In *North sea oil and gas reservoirs—ii* (p. 309-318). Springer  
397           Netherlands.
- 398 Cladouhos, T. T., & Marrett, R. (1996). Are fault growth and linkage models consistent  
399           with power-law distributions of fault lengths? *J. Struct. Geol.*, *18*, 281–  
400           293.
- 401 Clark, R. M., Cox, S., & Laslett, G. M. (1999). Generalizations of power-law distributions  
402           applicable to sampled fault-trace lengths: model choice, parameter  
403           estimation and caveats. *Geophys. J. Int.*, *136*(2), 357–372.
- 404 Clauset, A., Shalizi, C. R., & Newman, M. E. J. (2009). Power-law distributions in  
405           empirical data. *SIAM Review*, *51*(4), 661-703.
- 406 Cowie, P. A., & Scholz, C. H. (1992). Physical explanation for the displacement-  
407           length relationship of faults using a post-yield fracture mechanics model. *J.*  
408           *Struct. Geol.*, *14*, 1133–1148.
- 409 Cox, R. T., Van Arsdale, R. B., Harris, J. B., & Larsen, D. (2001). Neotectonics  
410           of the southeastern Reelfoot rift zone margin, central United States, and  
411           implications for regional strain accommodation. *Geology*, *29*(5), 419-422.

- 412 Cox, S., & Scholz, C. (1988). On the formation and growth of faults: an experimen-  
413 tal study. *J. Struct. Geol.*, *10*(4), 413-430.
- 414 Davis, K., Burbank, D. W., Fisher, D., Wallace, S., & Nobes, D. (2005). Thrust-  
415 fault growth and segment linkage in the active Ostler fault zone, New Zealand.  
416 *J. Struct. Geol.*, *27*(8), 1528-1546.
- 417 Dawers, N. H., & Anders, M. H. (1995). Displacement-length scaling and fault link-  
418 age. *J. Struct. Geol.*, *17*(5), 607-614.
- 419 Dokka, R. K., & Travis, C. J. (1990). Role of the Eastern California shear zone in  
420 accommodating Pacific-North American plate motion. *Geophys. Res. Lett.*, *17*,  
421 1323-1327.
- 422 Donath, F. A., & Parker, R. B. (1964). Folds and folding. *Geol. Soc. Am. Bull.*, *75*,  
423 45-62.
- 424 Eaton, G. P. (1982). The Basin and Range province: origin and tectonic significance.  
425 *Ann. Rev. Earth Planet. Sci.*, *10*(1), 409-440.
- 426 Fialko, Y. (2006). Interseismic strain accumulation and the earthquake potential on  
427 the southern San Andreas fault system. *Nature*, *441*, 968-971.
- 428 Fialko, Y. (2015). Fracture and Frictional Mechanics - Theory. In G. Schubert (Ed.),  
429 *Treatise on geophysics, 2nd. ed., vol. 4* (pp. 73-91). Elsevier Ltd., Oxford.
- 430 Fialko, Y. (2021). Estimation of absolute stress in the hypocentral region of the 2019  
431 Ridgecrest, California, earthquakes. *J. Geophys. Res.*, *126*, e2021JB022000.
- 432 Fialko, Y., & Jin, Z. (2021). Simple shear origin of the cross-faults ruptured in the  
433 2019 Ridgecrest earthquake sequence. *Nat. Geosci.*, *14*, 513-518.
- 434 Field, E. H., Arrowsmith, R. J., Biasi, G. P., Bird, P., Dawson, T. E., Felzer, K. R.,  
435 ... others (2014). Uniform California Earthquake Rupture Forecast, ver-  
436 sion 3 (UCERF3) The time-independent model. *Bull. Seism. Soc. Am.*, *104*,  
437 1122-1180.
- 438 Floyd, M., Funning, G., Fialko, Y. A., Terry, R. L., & Herring, T. (2020). Survey  
439 and Continuous GNSS in the vicinity of the July 2019 Ridgecrest earthquakes.  
440 *Seismol. Res. Lett.*, *91*, 2047-2054.
- 441 Fossen, H. (2020). Chapter 8 - fault classification, fault growth and displacement.  
442 In N. Scarselli, J. Adam, D. Chiarella, D. G. Roberts, & A. W. Bally (Eds.),  
443 *Regional geology and tectonics (second edition)* (p. 119-147). Elsevier.
- 444 Garthwaite, M. C., Wang, H., & Wright, T. J. (2013). Broad-scale interseismic de-

- 445 formation and fault slip rates in the central Tibetan Plateau observed using  
446 InSAR. *J. Geophys. Res.*, *118*(9), 5071–5083.
- 447 Gupta, A., & Scholz, C. H. (2000). Brittle strain regime transition in the Afar  
448 depression: Implications for fault growth and seafloor spreading. *Geology*,  
449 *28*(12), 1087–1090.
- 450 Hamiel, Y., Katz, O., Lyakhovsky, V., Reches, Z., & Fialko, Y. (2006). Stable and  
451 unstable damage growth in rocks with implications to fracturing of granite.  
452 *Geophys. J. Int.*, *167*, 1005–1016.
- 453 Hatcher, R. D. (1987). Tectonics of the Southern and Central Appalachian In-  
454 ternides. *Ann. Rev. Earth Planet. Sci.*, *15*(1), 337–362.
- 455 Hatton, C., Main, I., & Meredith, P. (1993). A comparison of seismic and structural  
456 measurements of scaling exponents during tensile subcritical crack growth. *J.*  
457 *Struct. Geol.*, *15*, 1485–1495.
- 458 Heifer, K., & Bevan, T. (1990). Scaling relationships in natural fractures-data, the-  
459 ory and applications. In *Proc. eur. petrol. conf.* (Vol. 2, pp. 367–376).
- 460 Herbert, J. W., Cooke, M. L., Oskin, M., & Difo, O. (2014). How much can off-  
461 fault deformation contribute to the slip rate discrepancy within the eastern  
462 California shear zone? *Geology*, *42*, 71–75.
- 463 Jia, Z., Jin, Z., Marchandon, M., Ulrich, T., Gabriel, A.-A., Fan, W., . . . others  
464 (2023). The complex dynamics of the 2023 Kahramanmaraş, Turkey, M w  
465 7.8–7.7 earthquake doublet. *Science*, *381*(6661), 985–990.
- 466 Jin, Z., Fialko, Y., Yang, H., & Li, Y. (2023). Transient deformation excited by the  
467 2021 M7.4 Maduo (China) earthquake: Evidence of a deep shear zone. *J. Geo-*  
468 *phys. Res.*, *128*, e2023JB026643.
- 469 Kaneko, Y., Fialko, Y., Sandwell, D., Tong, X., & Furuya, M. (2013). Interseismic  
470 deformation and creep along the central section of the North Anatolian Fault  
471 (Turkey): InSAR observations and implications for rate-and-state friction  
472 properties. *J. Geophys. Res.*, *118*(1), 316–331.
- 473 Katz, O., & Reches, Z. (2004). Microfracturing, damage, and failure of brittle gran-  
474 ites. *Journal of Geophysical Research: Solid Earth*, *109*(B1).
- 475 Kautz, S. A., & Sclater, J. G. (1988). Internal deformation in clay models of exten-  
476 sion by block faulting. *Tectonics*, *7*(4), 823–832.
- 477 King, G. C. P. (1983). The accomodation of large strains in the upper lithosphere of

- 478 the earth and other solids by self-similar fault systems: the geometric origin of  
 479 b-value. *Pure Appl. Geophys.*, *121*, 761–815.
- 480 Kostrov, B. V. (1974). Seismic moment and energy of earthquakes and seismic flow  
 481 of rock. *Izv., Acad. Sci., USSR, Phys. Solid Earth (Engl. Translation)*, *1*, 23–  
 482 40.
- 483 Krantz, R. W. (1988). Multiple fault sets and three-dimensional strain: Theory and  
 484 application. *J. Struct. Geol.*, *10*(3), 225-237.
- 485 Lindsey, E., & Fialko, Y. (2013). Geodetic slip rates in the Southern San Andreas  
 486 Fault System: Effects of elastic heterogeneity and fault geometry. *J. Geophys.*  
 487 *Res.*, *118*, 689–697.
- 488 Lindsey, E. O., & Fialko, Y. (2016). Geodetic constraints on frictional properties  
 489 and earthquake hazard in the Imperial Valley, Southern California. *J. Geophys.*  
 490 *Res.*, *121*, 1097–1113.
- 491 Lindsey, E. O., Sahakian, V. J., Fialko, Y., Bock, Y., Barbot, S., & Rockwell, T. K.  
 492 (2014). Interseismic strain localization in the San Jacinto fault zone. *Pure and*  
 493 *Applied Geophysics*, *171*(11), 2937–2954.
- 494 Lisowski, M., Savage, J., & Prescott, W. H. (1991). The velocity field along the San  
 495 Andreas fault in central and southern California. *J. Geophys. Res.*, *96*, 8369–  
 496 8389.
- 497 Louderback, G. D. G. D. (1950). *Faults and engineering geology*. United States: Ge-  
 498 ological Society of America.
- 499 Mansfield, C., & Cartwright, J. (2001). Fault growth by linkage: observations and  
 500 implications from analogue models. *J. Struct. Geol.*, *23*(5), 745-763.
- 501 Marrett, R., & Allmendinger, R. W. (1991). Estimates of strain due to brittle fault-  
 502 ing: sampling of fault populations. *J. Struct. Geol.*, *13*, 735–738.
- 503 Marrett, R., & Allmendinger, R. W. (1992). Amount of extension on "small" faults:  
 504 An example from the Viking graben. *Geology*, *20*, 47–50.
- 505 Nicol, A., Walsh, J., Watterson, J., & Gillespie, P. (1996). Fault size distributions —  
 506 are they really power-law? *J. Struct. Geol.*, *18*(2), 191-197.
- 507 NJ Dept. of Environmental Protection Bureau of GIS. (2023). *Geologic faults in*  
 508 *New Jersey*.
- 509 Odling, N., Gillespie, P., Bourguine, B., Castaing, C., Chiles, J., Christensen, N., ...  
 510 others (1999). Variations in fracture system geometry and their implications

- 511 for fluid flow in fractures hydrocarbon reservoirs. *Petroleum Geoscience*, *5*,  
512 373–384.
- 513 Ojo, O. O., Ohenhen, L. O., Kolawole, F., Johnson, S. G., Chindandali, P. R., Atek-  
514 wana, E. A., & Lao-Davila, D. A. (2022). Under-displaced normal faults:  
515 Strain accommodation along an early-stage rift-bounding fault in the Southern  
516 Malawi Rift. *Frontiers in earth science*, *10*.
- 517 PA Department of Conservation & Natural Resources. (2023). *Bedrock geology of*  
518 *Pennsylvania - faults (vector)*.
- 519 Pan, S., Naliboff, J., Bell, R., & Jackson, C. (2023). How do rift-related fault net-  
520 work distributions evolve? quantitative comparisons between natural fault  
521 observations and 3D numerical models of continental extension. *Tectonics*,  
522 *42*(10), e2022TC007659.
- 523 Pancha, A., Anderson, J. G., & Kreemer, C. (2006). Comparison of seismic and  
524 geodetic scalar moment rates across the Basin and Range Province. *Bull.*  
525 *Seism. Soc. Am.*, *96*, 11–32.
- 526 Proekt, A., Banavar, J. R., Maritan, A., & Pfaff, D. W. (2012). Scale invariance  
527 in the dynamics of spontaneous behavior. *Proc. Natl. Acad. Sci.*, *109*, 10564–  
528 10569.
- 529 Riznichenko, Y. V. (1965). The flow of rocks as related to seismicity. *Dokl. Akad.*  
530 *Nauk SSSR*, *161*(1), 96–98.
- 531 Roman, S., & Bertolotti, F. (2022). A master equation for power laws. *Royal Society*  
532 *Open Science*, *9*(12), 220531.
- 533 Ron, H., Beroza, G., & Nur, A. (2001). Simple model explains complex faulting.  
534 *Eos, Transactions American Geophysical Union*, *82*(10), 125–129.
- 535 Rotevatn, A., Jackson, C. A.-L., Tvedt, A. B., Bell, R. E., & Blækkan, I. (2019).  
536 How do normal faults grow? *J. Struct. Geol.*, *125*, 174–184.
- 537 Rui, X., & Stamps, D. S. (2019). Strain accommodation in the Daliangshan moun-  
538 tain area, southeastern margin of the Tibetan Plateau. *J. Geophys. Res. Solid*  
539 *Earth*, *124*(9), 9816–9832.
- 540 Schmalzle, G., Dixon, T., Malservisi, R., & Govers, R. (2006). Strain accumulation  
541 across the Carrizo segment of the San Andreas Fault, California: Impact of  
542 laterally varying crustal properties. *J. Geophys. Res.*, *111*, B05403.
- 543 Scholz, C., Dawers, N., Yu, J.-Z., Anders, M., & Cowie, P. (1993). Fault growth and

- 544 fault scaling laws: Preliminary results. *J. Geophys. Res.*, *98*, 21951–21961.
- 545 Scholz, C. H., & Cowie, P. A. (1990). Determination of total strain from faulting us-  
546 ing slip measurements. *Nature*, *346*(6287), 837–839.
- 547 Segall, P. (2002). Integrating geologic and geodetic estimates of slip rate on the San  
548 Andreas fault system. *Int. Geol. Rev.*, *44*, 62–82.
- 549 Segall, P., & Pollard, D. D. (1983). Joint formation in granitic rock of the Sierra  
550 Nevada. *GSA Bulletin*, *94*(5), 563–575.
- 551 Sornette, A., Davy, P., & Sornette, D. (1993). Fault growth in brittle-ductile ex-  
552 periments and the mechanics of continental collisions. *J. Geophys. Res.*, *98*,  
553 12111–12139.
- 554 Stumpf, M. P., & Porter, M. A. (2012). Critical truths about power laws. *Science*,  
555 *335*, 665–666.
- 556 Tatar, O., Poyraz, F., Gürsoy, H., Cakir, Z., Ergintav, S., Akpınar, Z., . . . others  
557 (2012). Crustal deformation and kinematics of the Eastern Part of the North  
558 Anatolian Fault Zone (Turkey) from GPS measurements. *Tectonophysics*, *518*,  
559 55–62.
- 560 Torabi, A., & Berg, S. S. (2011). Scaling of fault attributes: A review. *Marine and*  
561 *Petroleum Geology*, *28*(8), 1444–1460.
- 562 Turcotte, D. (1986). A fractal model for crustal deformation. *Tectonophysics*,  
563 *132*(1), 261–269.
- 564 Tymofyeyeva, E., & Fialko, Y. (2015). Mitigation of atmospheric phase delays in In-  
565 SAR data, with application to the Eastern California Shear Zone. *J. Geophys.*  
566 *Res.*, *120*, 5952–5963.
- 567 Tymofyeyeva, E., & Fialko, Y. (2018). Geodetic evidence for a blind fault segment  
568 at the Southern end of the San Jacinto Fault Zone. *J. Geophys. Res.*, *123*,  
569 878–891.
- 570 Tymofyeyeva, E., Fialko, Y., Jiang, J., Xu, X., Sandwell, D., Bilham, R., . . .  
571 Moafipoor, S. (2019). Slow slip event on the southern San Andreas fault  
572 triggered by the 2017  $M_w$ 8.2 Chiapas (Mexico) earthquake. *J. Geophys. Res.*,  
573 *124*, 9956–9975.
- 574 U.S. Geological Survey and Nevada Bureau of Mines and Geology. (2023). *Quater-*  
575 *nary fault and fold database for the united states, accessed mar 1.*
- 576 Vavra, E. J., Qiu, H., Chi, B., Share, P.-E., Allam, A., Morzfeld, M., . . . Fialko, Y.

- 577 (2023). Active dipping interface of the Southern San Andreas fault revealed by  
578 space geodetic and seismic imaging. *J. Geophys. Res.*, *128*, e2023JB026811.
- 579 Villemain, T., Angelier, J., & Sunwoo, C. (1995). Fractal distribution of fault length  
580 and offsets: Implications of brittle deformation evaluation—The Lorraine coal  
581 basin. In C. C. Barton & P. R. La Pointe (Eds.), *Fractals in the earth sciences*  
582 (pp. 205–226). Boston, MA: Springer US.
- 583 Walsh, J., Watterson, J., & Yielding, G. (1991). The importance of small-scale fault-  
584 ing in regional extension. *Nature*, *351*, 391–393.
- 585 Walsh, J. J., & Watterson, J. (1988). Analysis of the relationship between displace-  
586 ments and dimensions of faults. *J. Struct. Geol.*, *10*, 239–247.
- 587 Wang, M., & Shen, Z.-K. (2020). Present-day crustal deformation of continen-  
588 tal China derived from GPS and its tectonic implications. *J. Geophys. Res.*,  
589 *125*(2), e2019JB018774.
- 590 Wessel, P., Smith, W. H. F., Scharroo, R., Luis, J., & Wobbe, F. (2013). Generic  
591 Mapping Tools: Improved Version Released. *Eos, Trans. AGU*, *94*, 409–410.
- 592 Woessner, J., & Wiemer, S. (2005). Assessing the quality of earthquake catalogues:  
593 Estimating the magnitude of completeness and its uncertainty. *Bull. Seism.*  
594 *Soc. Am.*, *95*(2), 684–698.
- 595 Zou, X., Fialko, Y., Dennehy, A., Cloninger, A., & Semnani, S. J. (2023). High-angle  
596 active conjugate faults in the Anza-Borrego Shear Zone, Southern California.  
597 *Geophys. Res. Lett.*, *50*, e2023GL105783.

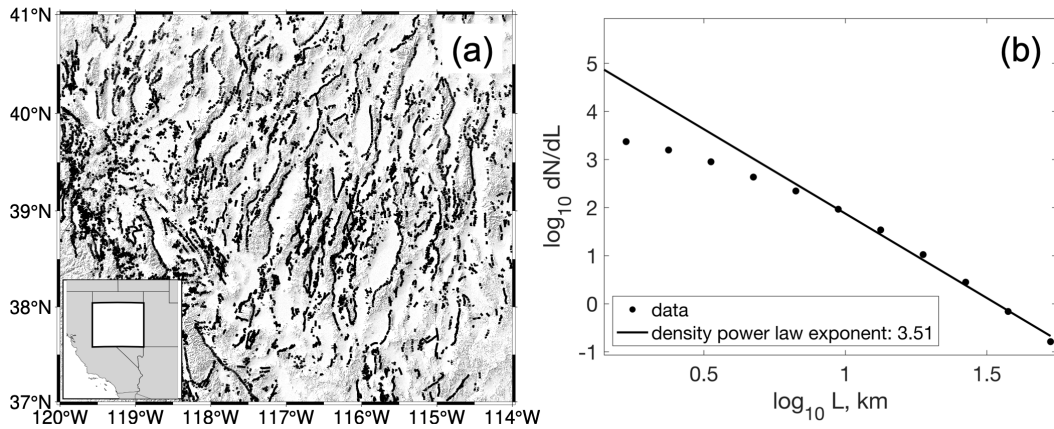


**Figure 1.** (a) Map of the Basin and Range Province. Shading denotes topography. Black lines denote fault traces. Inset shows location of the area of interest (white rectangle) in a regional context; thin black lines indicate state boundaries. The concatenated fault data set includes 10825 fault segments. The minimum segment length is 2.1 m and the maximum length is 49 km. (b): Probability density of the fault length distribution, on a log-log scale. Solid line represents the best linear fit at the high end of the fault length distribution ( $L > 5$  km). The estimated power-law exponent (slope of the best-fit line) is  $\beta = 3.51 \pm 0.12$ .

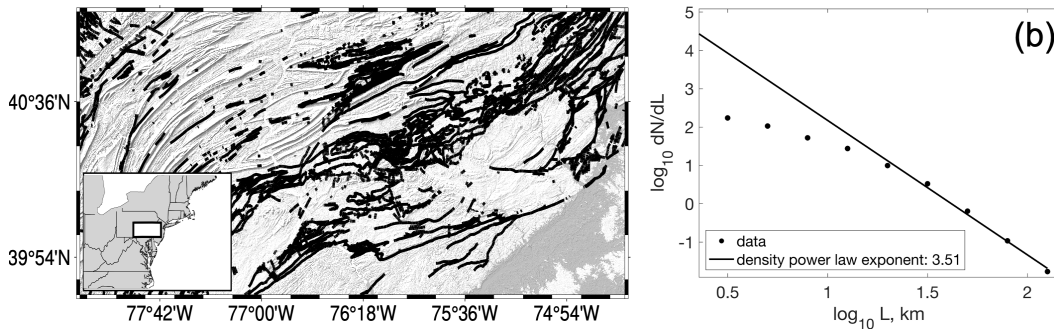


**Figure 2.** (a) Map of Central Pennsylvania and Northern New Jersey. Notation is the same as in Figure 1. The concatenated fault data set includes 2273 fault segments. The minimum segment length is 15 m and the maximum length is 108 km. (b) Probability density of the fault length distribution, on a log-log scale. Solid line represents the best linear fit at the high end of the fault length distribution ( $L > 10$  km). The estimated power-law exponent (slope of the best-fit line) is  $\beta = 3.51 \pm 0.20$ .

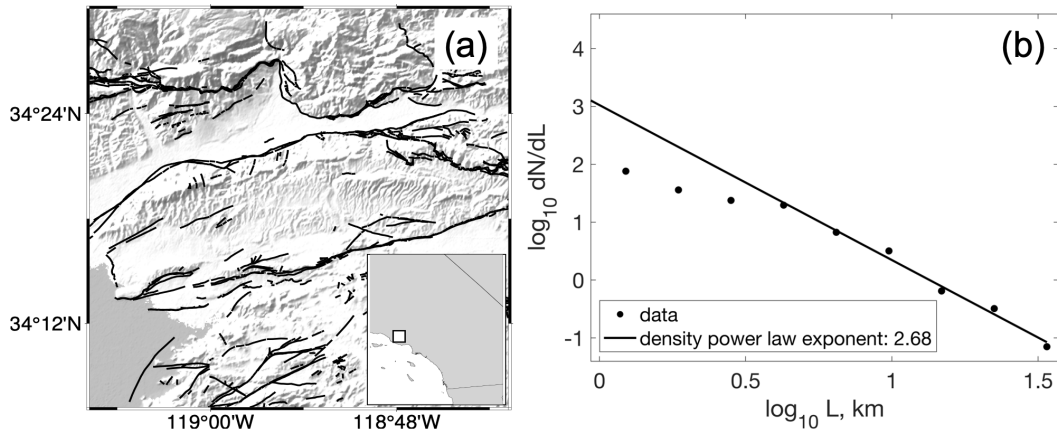


**Figure 3.** (a) Map of Ventura County, CA. Notation is the same as in Figure 1. The concatenated fault data set includes 349 fault segments. The minimum segment length is 0.6 m and the maximum length is 30 km. (b) Probability density of the fault length distribution, on a log-log scale. Solid line represents the best linear fit at the high end of the fault length distribution ( $L > 3$  km). The estimated power-law exponent (slope of the best-fit line) is  $\beta = 2.68 \pm 0.14$ .

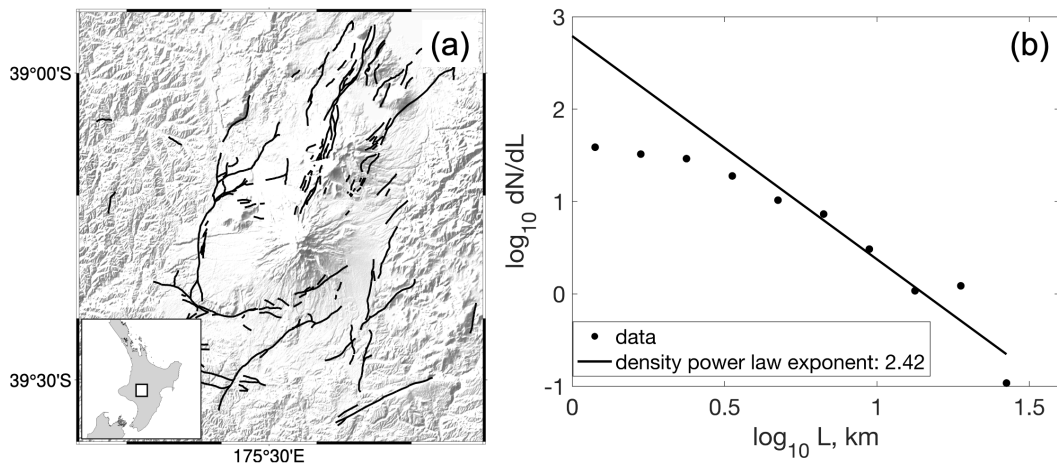


**Figure 4.** (a) Map of Northern New Zealand. Notation is the same as in Figure 1. The concatenated fault data set includes 159 fault segments. The minimum segment length is 363 m and the maximum length is 24.7 km. (b) Probability density of the fault length distribution, on a log-log scale. The solid line represents the best linear fit at the high end of the fault length distribution ( $L > 4$  km). The estimated power-law exponent (slope of the best-fit line) is  $\beta = 2.42 \pm 0.35$ .

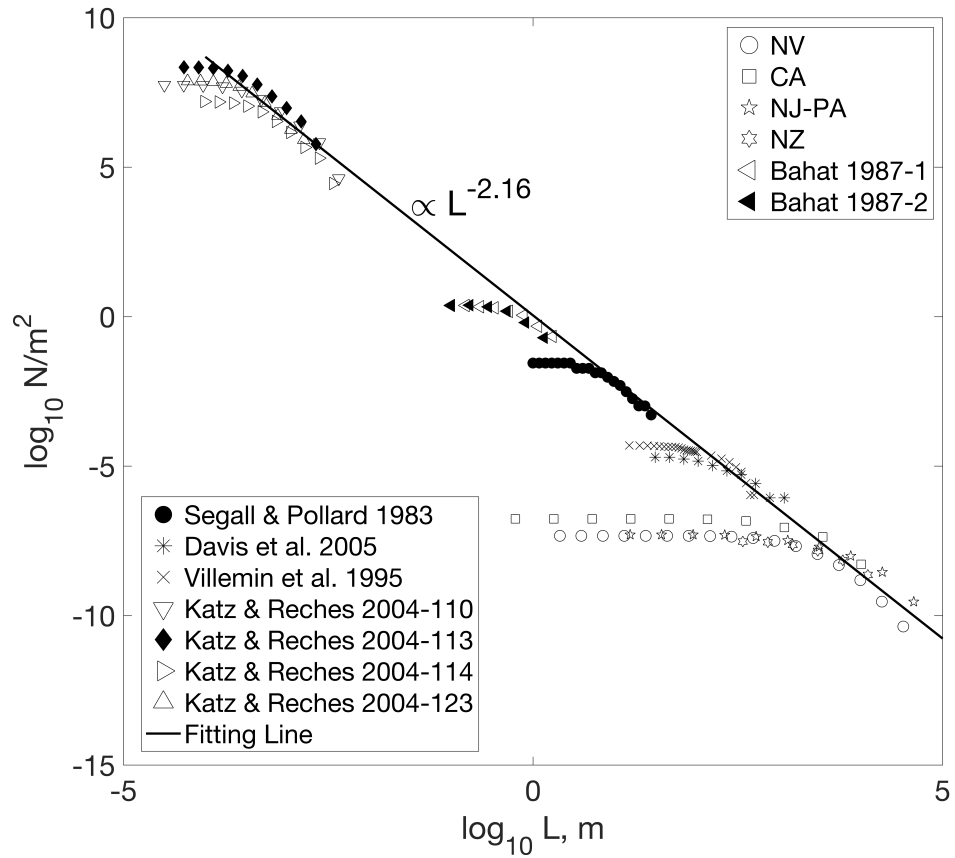


**Figure 5.** Cumulative fault length frequency distribution for a combined data set including fault traces (Figures 1-4), as well as outcrop-scale and lab data, normalized by the respective observation areas, on a log-log scale. The solid line is the least-squares fit for the "high-end" asymptotes of all constituent data sets. The estimated power-law exponent is  $\alpha = 2.16$ .

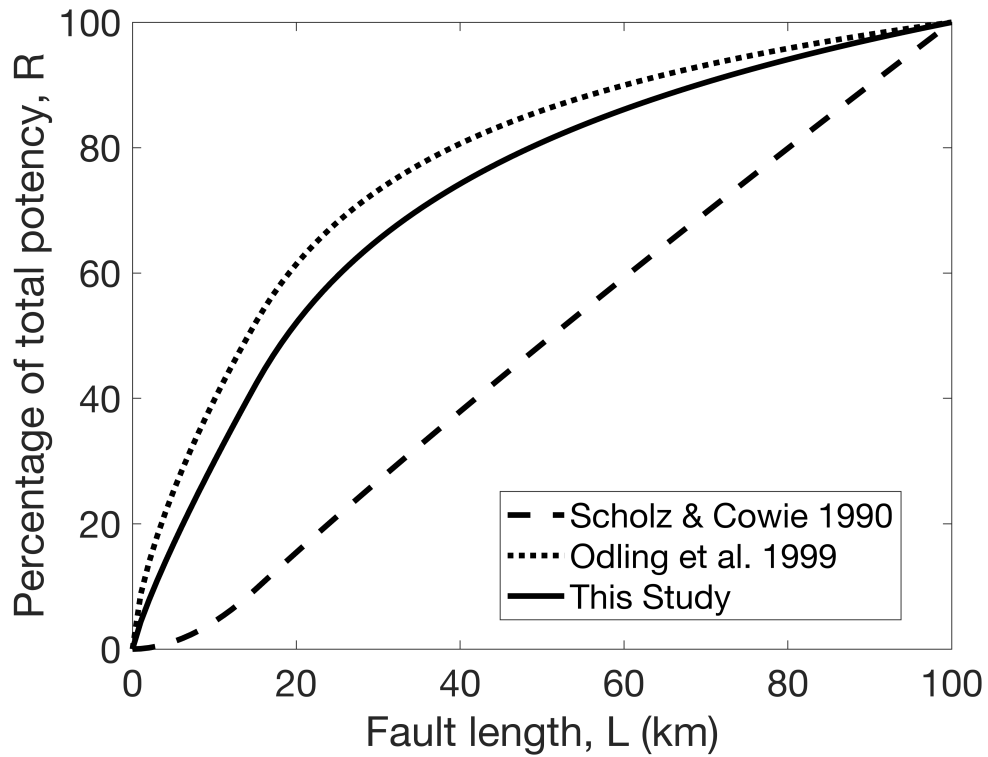


**Figure 6.** Percentage of the total potency  $R$  (equation 8) accommodated by faults having length less than  $L$ , for several estimated values of the power-law exponent  $\alpha$ : solid line,  $\alpha = 2.16$  (this study); dotted line,  $\alpha = 2.34$  (Odling et al., 1999); dashed line,  $\alpha = 1.1$  (C. H. Scholz & Cowie, 1990). We assume  $L_{max} = 100$  km (Figure 5).

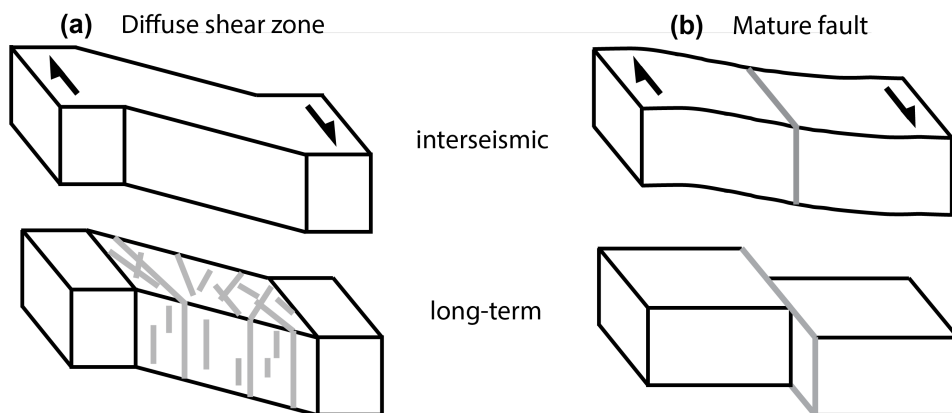


**Figure 7.** Schematic representation of kinematics of (a) developing shear zone and (b) mature plate boundary fault. Top and bottom panels denote interseismic and long-term (averaged over multiple earthquake cycles) motion, respectively. Gray lines denote active faults.

Figure 1.

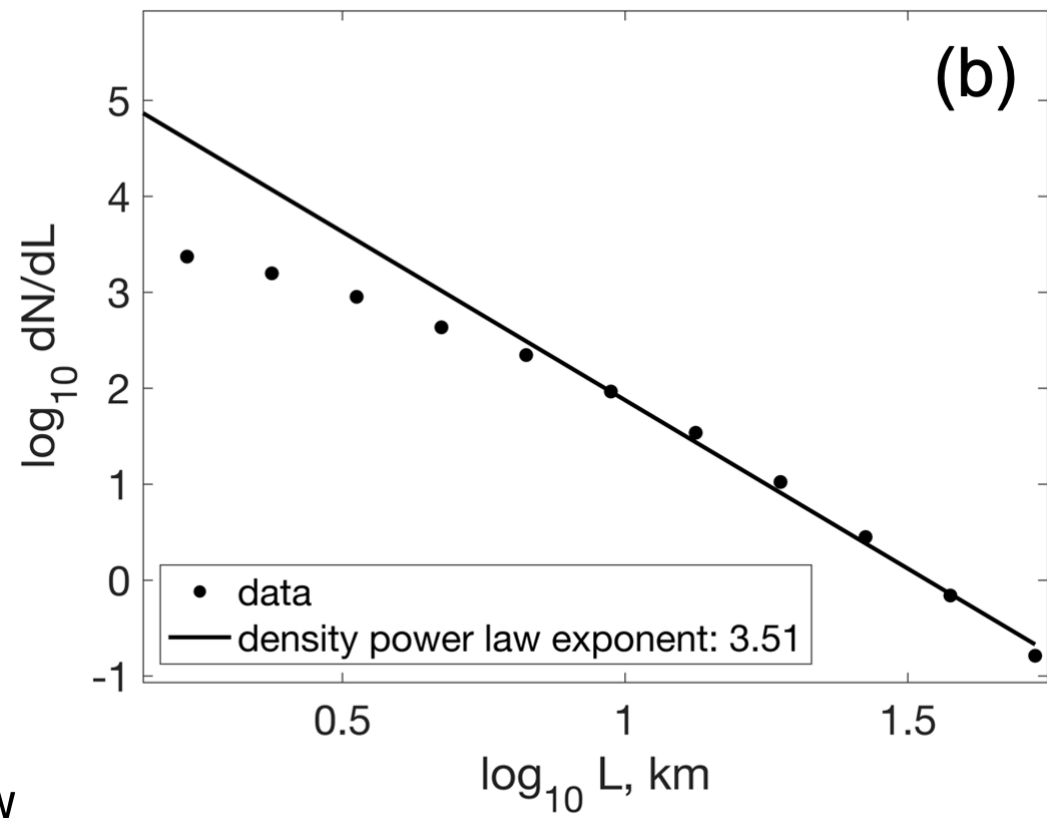
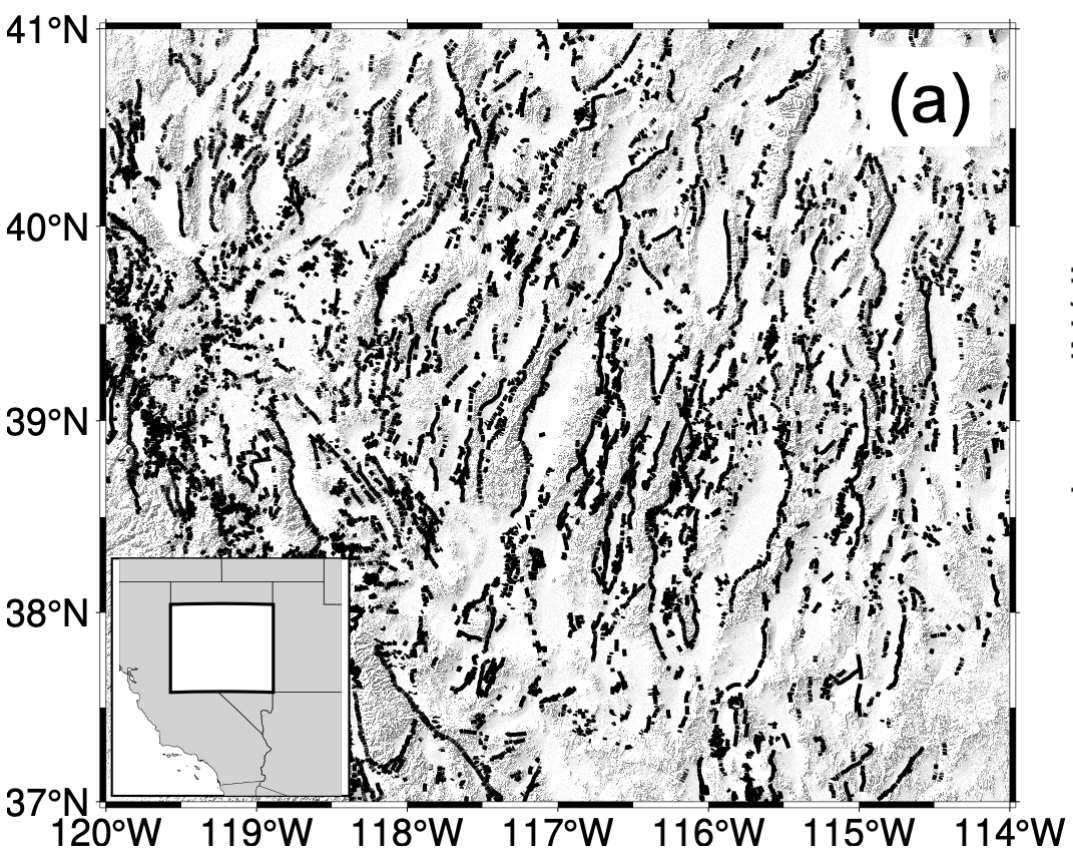


Figure 2.

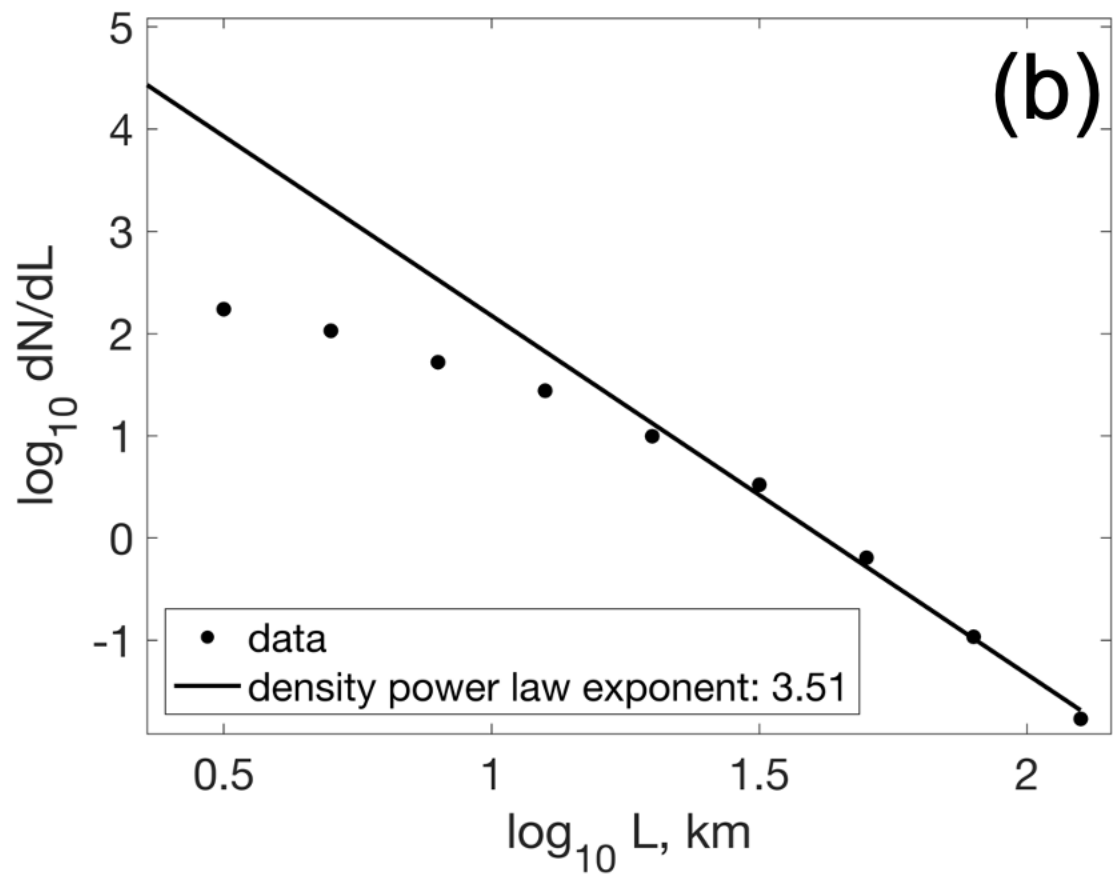
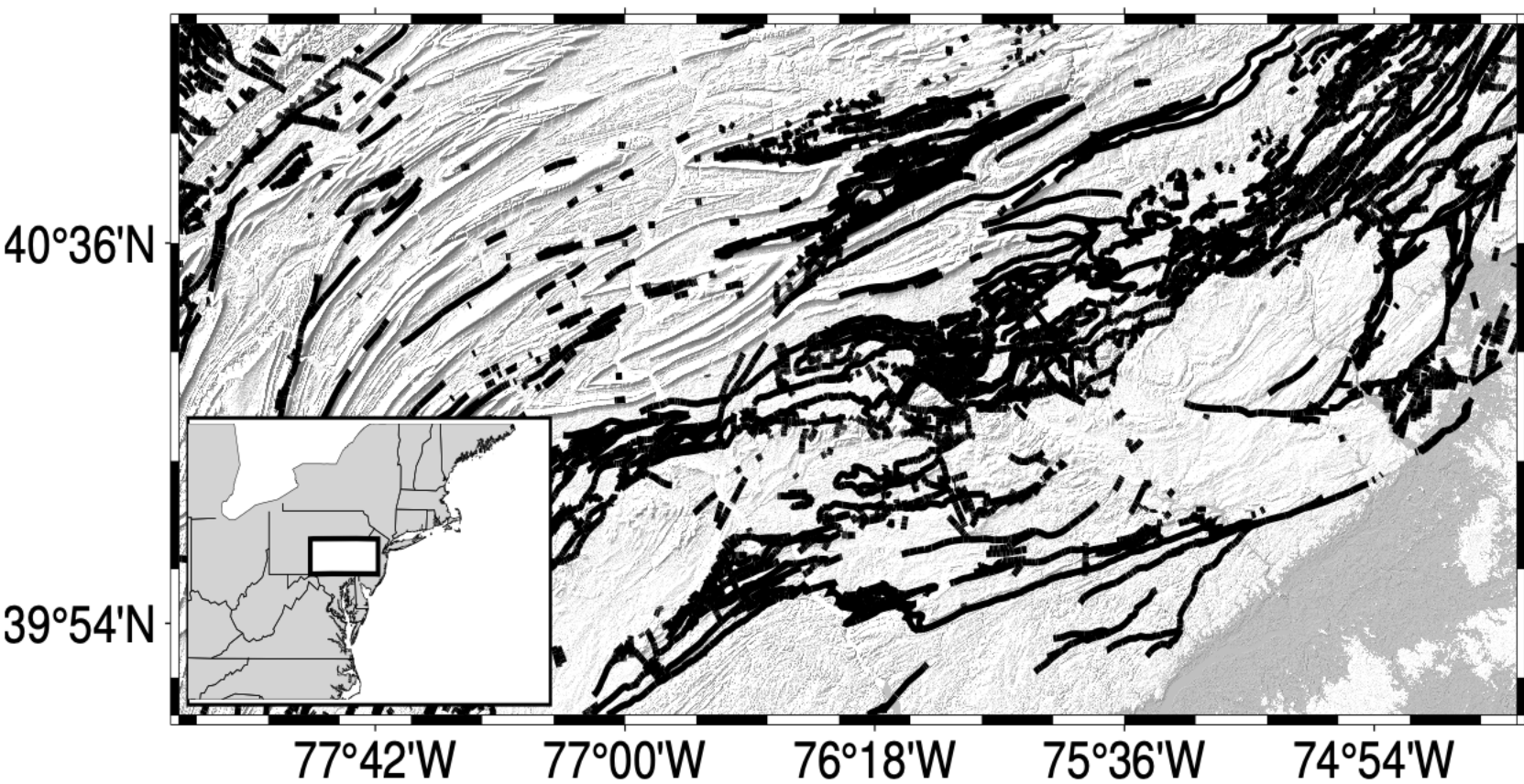


Figure 3.

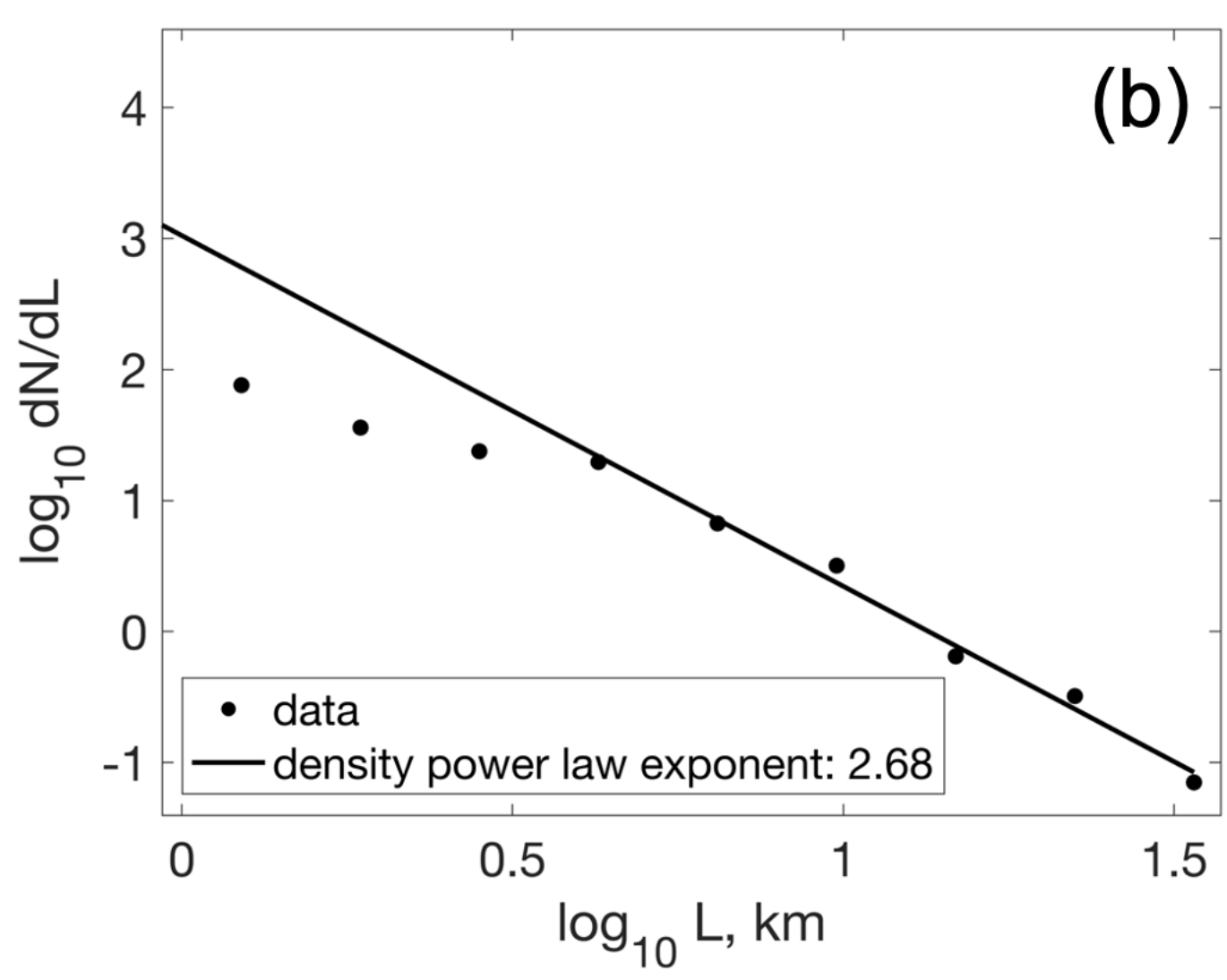
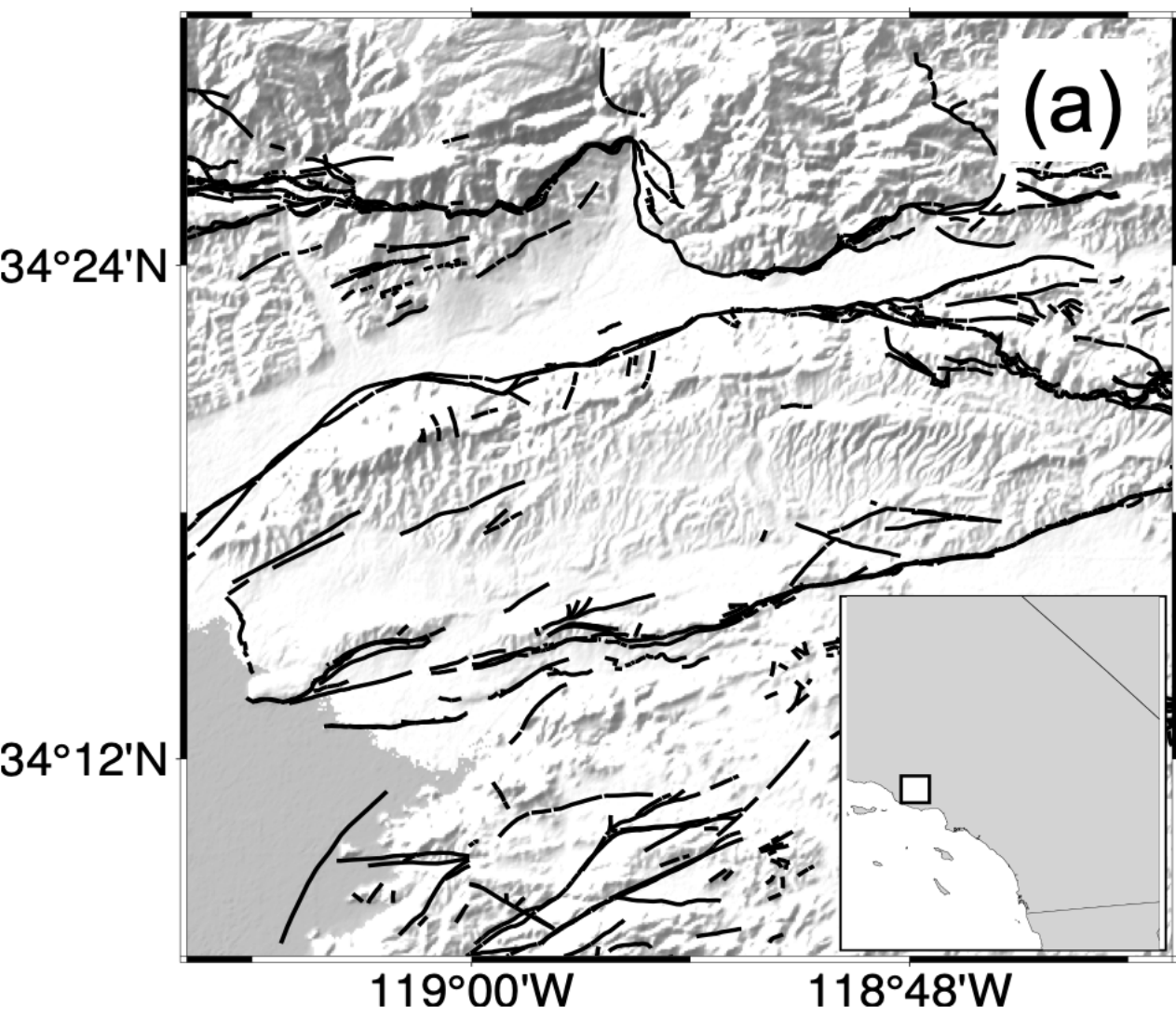


Figure 4.

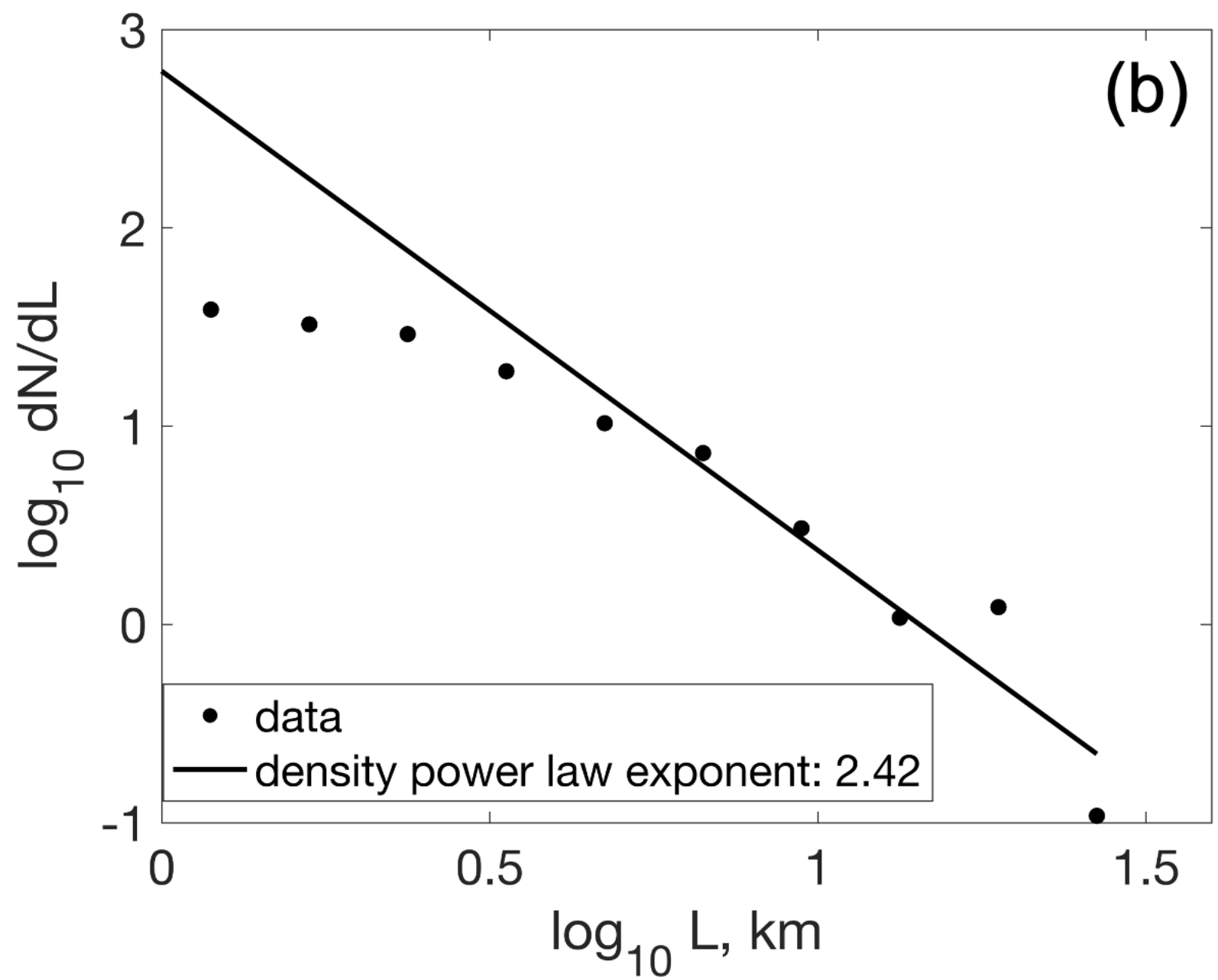
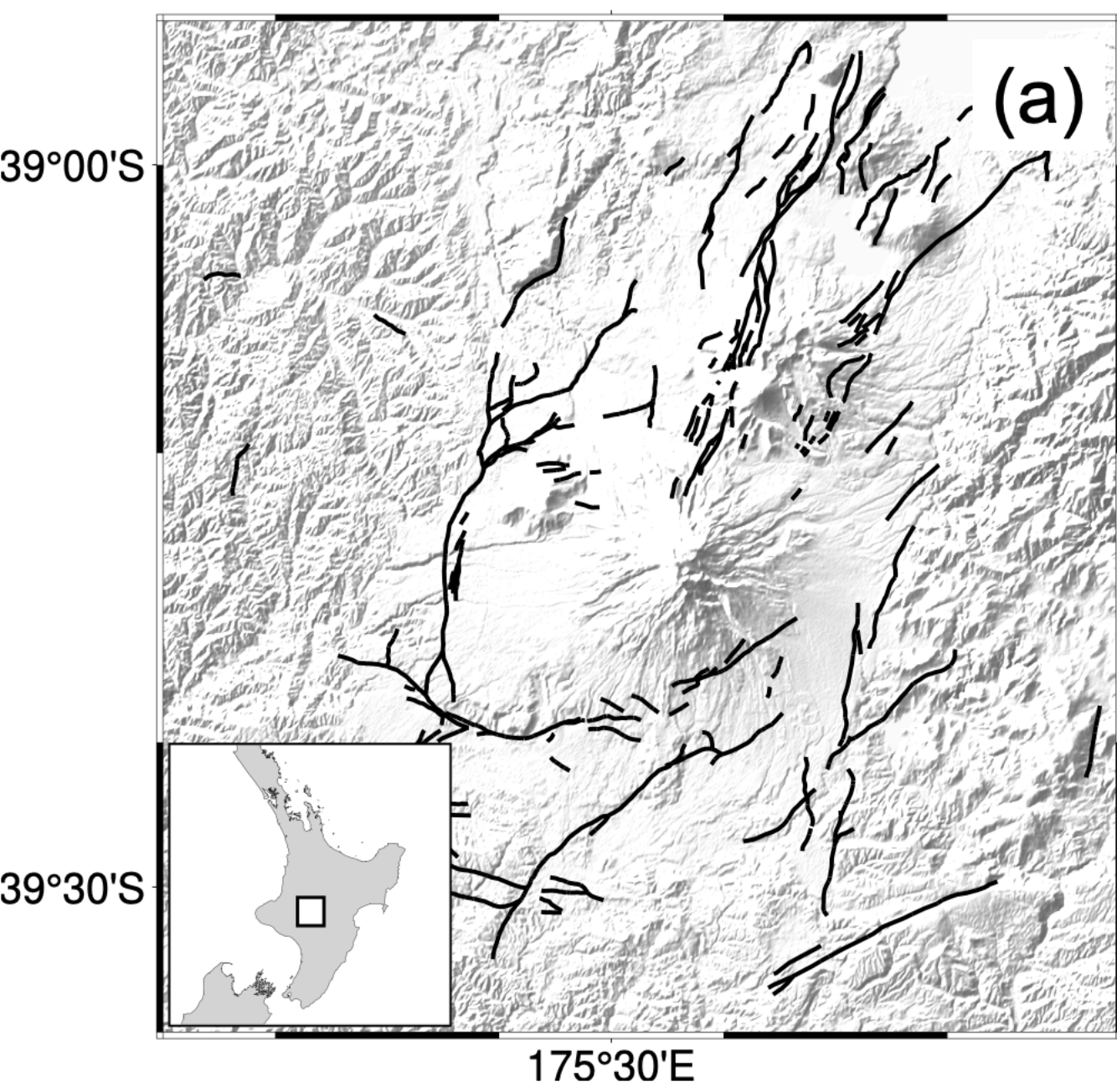


Figure 5.

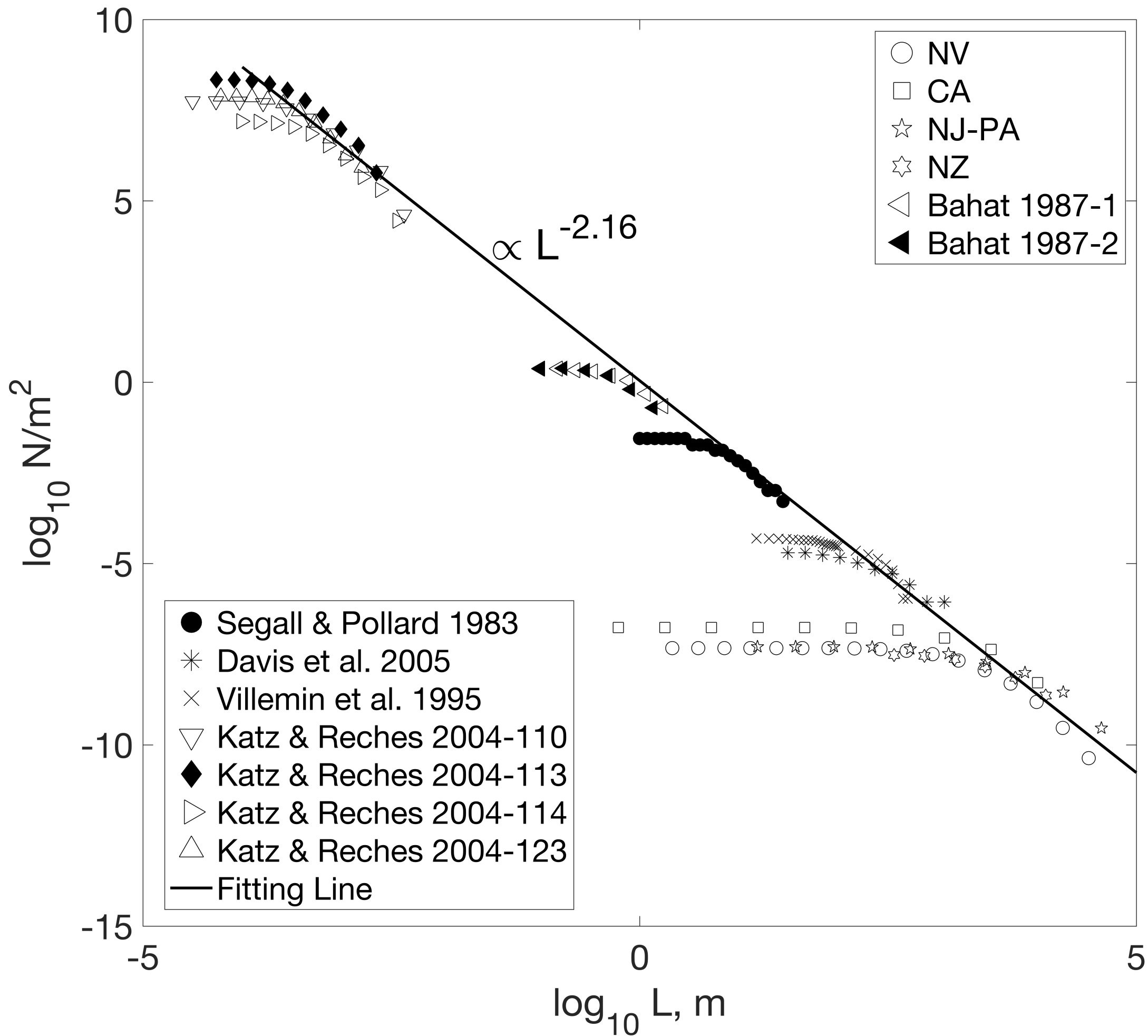


Figure 6.

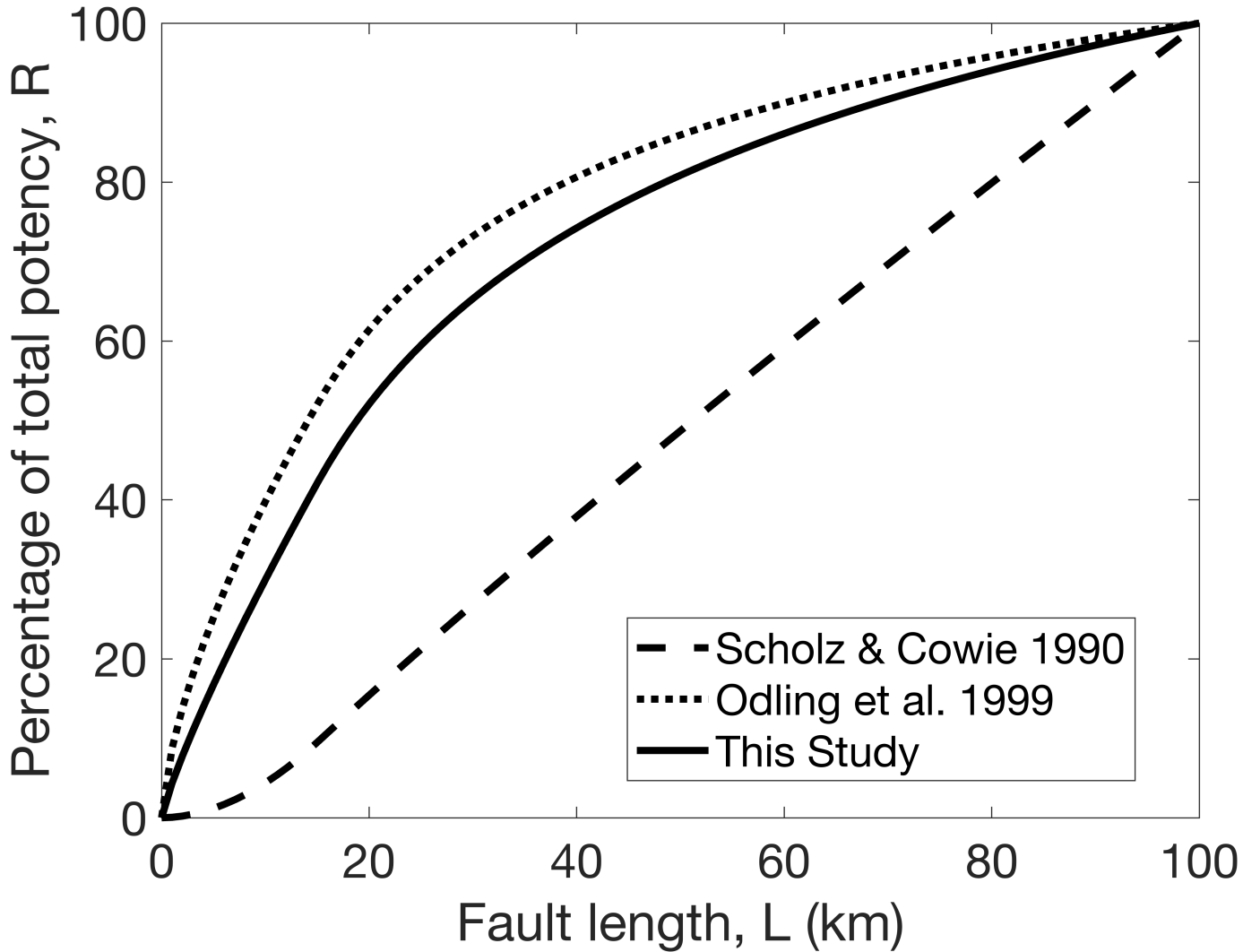
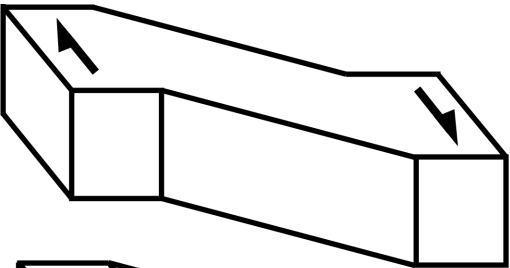


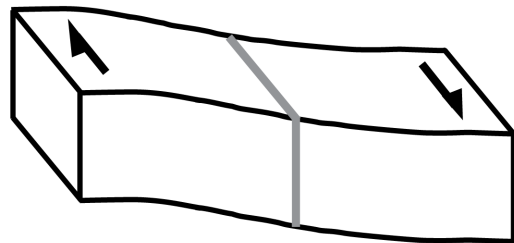
Figure 7.

**(a)** Diffuse shear zone



interseismic

**(b)** Mature fault



long-term

